UNIVERSITY OF CALIFORNIA
RIVERSIDE

Wide Band Gap Single Wurtzite Ternary Alloy MgZnO Thin Film Grown by MBE

A Thesis submitted in partial satisfaction
of the requirements for the degree of

Master of Science

in

Materials Science and Engineering

by

Shyue-Shiun Chiang

December 2019

Thesis Committee:

Dr. Jianlin Liu, Chairperson
Dr. Pingyun Feng
Dr. Ruoxue Yan

The Thesis of Shyue-Shiun Chiang is approved:

_____

_____

_____

Committee Chairperson

University of California, Riverside

To my parents, PI and lab mates for all their love and support.

ABSTRACT OF THE THESIS

Wide Band Gap Single Wurtzite Ternary Alloy MgZnO Thin Film Grown by MBE

by

Shyue-Shiun Chiang

Master of Science, Graduate Program in Materials Science and Engineering
University of California, Riverside, December 2019
Dr. Jianlin Liu, Chairperson

Ternary alloy MgZnO thin film on c-plane sapphire was obtained by radio-frequency (RF) plasma-assisted molecular beam epitaxy (MBE). The films were characterized by photoluminescence (PL), UV-visible absorption and X-ray diffraction (XRD). The band gaps of ZnO based MgZnO ternary alloy thin films were tuned from 3.71eV to 4.2eV at room temperature, and these films remain single wurtzite structure. The band gaps were determined by Tauc plot of the absorption spectrum. High magnesium content ZnO based MgZnO ternary alloy thin films were achieved by controlling substrate temperature, effusion cell temperature and buffer layer conditions. In this thesis we mainly investigated single wurtzite MgZnO ternary alloy as wide band gap ZnO based semiconductor material for fabricating optoelectronic devices.

Table of Contents

List of Figures

List of Tables

Chapter 1

Introduction

1.1 ZnO

The growth and characterization of II-VI semiconductor zinc oxide (ZnO) were widely reported during the past few decades due to its wide band gap energy property. As a promising deep UV semiconductor material, it can be used for various applications such as light emitting diode (LED), laser diode, ultraviolet photodetector, gas sensor and so on. ZnO has a wide band gap of 3.37 eV and a large binding energy of 60 meV at room temperature. Table 1.1 shows the comparison of the properties of ZnO with other wide band gap semiconductor materials [1]. ZnO has the highest exciton binding energy among all the materials in Table 1.1, the binding energy of ZnO is almost three times larger than the commercialized semiconductor material GaN which has a binding energy of 21 meV. Excitonic recombination is preferable because the exciton is already a bound system, the exciton recombines more efficiently without requiring traps to localize carrier. It allows the exciton to dominate recombination process. Moreover, the deeper exciton of ZnO is more steady against field ionization that cause by piezoelectrically induced fields [2]. The large exciton binding energy also allows the excitonic emission in ZnO to occur at room temperature or even higher temperature. ZnO crystallizes in two different forms which are hexagonal wurtzite and cubic zincblende. The wurtzite structure of ZnO is the most common crystal structure since it is more stable at ambient condition. This is different with GaN which is more appear with zincblende structure.

However, ZnO is more available for large bulk single crystal [3]. ZnO crystal usually has n-type conductivity without any doping, the native point defects (i.e. vacancies, interstitials and antisites) and the incorporation of impurities play an important role in the conductivity of ZnO. In the past few decades, it was considered that the unintentional n-type conductivity of ZnO is caused by oxygen vacancies or zinc interstitials defects [4]. Some recent reports show that the oxygen vacancies cannot contribute to unintentional n-type conductivity by using density functional theory calculations [5, 6]. The calculation shows that the oxygen vacancy of ZnO is a deep donor instead of a shallow donor. However, the latest report indicates that the unintentional n-type conductivity of ZnO is due to oxygen vacancies native point defects by investigating the self-diffusion process of oxygen atoms [7]. ZnO is an unintentional n-type conductivity semiconductor material, it can be doped as a strong n-type or a p-type material with different dopants. Table 1.2 shows the properties of different dopant impurities in ZnO [8]. For the n-type doping, the most common dopants (donor impurities) are group III impurities, fluorine and hydrogen. On the other hand, the most common dopants (acceptor impurities) for p-type doping are group I impurities, group V impurities, copper and nitrogen. As a semiconductor material, the band gap engineering plays a very important role. The band gap engineering in ZnO can be achieved by alloying with MgO and CdO, the bad gap can be tuned to larger and smaller individually. In this thesis, we focus on the wide band gap tuning of MgZnO ternary alloy.

1.2 MgZnO

In the past few decades, MgZnO ternary alloy was studied widely as a wide band gap semiconductor material due to the potential substitute of GaN by ZnO for optoelectronics applications. ZnO has direct band gap energy of 3.37 eV at room temperature whereas MgO has band gap energy of 7.8 eV at room temperature. Since the ionic radius of Mg^{2+} (0.57 Å) is similar to Zn^{2+} (0.6 Å), the replacement of Zn by Mg should not lead to a significant change in the lattice constants. However, ZnO has a stable hexagonal wurtzite structure while MgO has cubic structure, as shown in figure 1.1 [9]. This leads to a significant challenge for Mg incorporation of ZnO. As the Mg incorporation content increases, the crystal structure of the ternary alloy MgZnO will emerge phase transition. Figure 1.2 shows the 2 × 2 × 2 hexagonal wurtzite ZnO supercell doped with Mg replacing the Zn position [10]. Red, blue and green spheres represent O, Zn and Mg atoms respectively. The Mg concentration x increases 0.0625 while every single Zn atom is substituted by an Mg atom with the molecular formula $Mg_xZn_{1-x}O$. Although the ionic radius of Zn^{2+} is similar to Mg^{2+}, a large lattice constant difference between wurtzite hexagonal ZnO (a = 3.25 Å and c = 5.21 Å) and rock salt MgO (a = 4.21 Å) can lead to unstable mixed phase. Recently, it has been reported that MgZnO thin film can be grown with Mg concentration up to 33 mol% without phase separation, which is corresponding to band gap energy of 4.0 eV [11]. From the calculation we know that MgZnO with 33 mol% of Mg concentration is approximately equal to 5 to 6 Zn atoms substituted by Mg

atoms in every 16 Zn atoms inside a 2 × 2 × 2 hexagonal wurtzite ZnO supercell. Table 1.3 shows the calculated lattice constants of the hexagonal and cubic $Mg_xZn_{1-x}O$ [9]. Since the ionic radius of Mg^{2+} is slightly smaller than Zn^{2+}, the lattice constant decreases as the Mg incorporation increases. Figure 1.3 shows the relationship between band gap energy and Mg content in $Mg_xZn_{1-x}O$ thin film [12]. $Mg_xZn_{1-x}O$ thin film grown on c-plane sapphire can have single hexagonal wurtzite structure of Mg composition up to 37% without phase separation. Once the Mg composition is larger than 37%, the cubic phase crystal will start to emerge. When Mg composition is in the region from 37% to 62%, $Mg_xZn_{1-x}O$ thin film has mixed phases of hexagonal wurtzite and cubic crystal structure. As the Mg composition increases up to 62%, the crystal structure of $Mg_xZn_{1-x}O$ thin film will turn into single cubic phase. The band gap energy of $Mg_xZn_{1-x}O$ ternary alloy for Mg concentration below 40% (not applicable for x larger than 0.4 or band gap larger than 4.28 eV) can approximately be calculated by the following equation [13] :

$$E_g = 3.35 + 2.33x$$

In this thesis, we focus on the wide band gap single wurtzite structure MgZnO ternary alloy thin film growth as a promising deep UV region semiconductor material.

1.3 Molecular beam epitaxy

Molecular beam epitaxy (MBE) is an epitaxial growth method of semiconductors and other films which was developed in the late 1960s at Bell Telephone Laboratories by J. R. Arthur and Alfred Y. Cho [14]. In the MBE system, thin films crystallize through the reactions between the constituent elements on the hot substrate surface under ultra-high

vacuum condition. The base pressure of the MBE chamber usually remains lower than 10^{-9} Torr. In Quantum Structures Lab (QSL), we use a customized built SVTA MBE system for thin films growth, as shown in Figure 1.4. The molecular beam epitaxy system consists of many components which are load lock chamber, main chamber, effusion cells, RF plasma and so on. The two chambers are connected to each other with a gate valve. The first chamber is load lock chamber, which has a pressure of ~10^{-7} Torr maintained with mechanical pump and molecular turbo pump. The mechanical pump can first pump to ~10^{-3} Torr and the molecular turbo pump can further pump to ~10^{-7} Torr. The main function of load lock chamber is to load the sample which is placed on the holder. The second chamber is main chamber, also known as growth chamber. The mechanical pump can first pump to ~10^{-3} Torr and the molecular turbo pump can further pump to ~10^{-9} - 10^{-10} Torr. There is an additional ion pump connecting to the main chamber to absorb the inert, lighter and other gases. The growth rate of molecular beam epitaxy is approximately up to 1 μm per hour, which is low enough for surface migration of the impinging species on the growing surface. This allows the surface of the thin film to be very smooth, it also provides atomic accuracy and controllability for achieving high quality thin films. Figure 1.5 shows the schematic of molecular beam epitaxy system in Quantum Structures Lab. The element sources are stored in different quasi-Knudsen effusion cells. Before the growth, the effusion cells and the substrate heater were heated up to a specific temperature, the temperature precision of effusion cells and substrate

heater are both 1 ˚C. During the growth, the on-and-off condition of diffused elements is controlled by compressed air physical shutter. As the effusion cell starts to heat up, the solid source inside the crucible of the effusion cell begin to slowly evaporate. The sublimed gaseous elements then form as molecular beam, which condense on the wafer directly without interaction with other atoms due to the long mean free paths under ultra-high vacuum ambient condition. The molecular beam inside the MBE chamber can be basically divided into three zones, as shown in Figure 1.5 [15]. The first zone is the generation zone of the molecular beams, where the gaseous beams travel without interaction with other beams. The second zone is the vapor elements mixing zone, where the gaseous beams from different effusion cells intersect with each other. The last zone is the substrate crystallization zone, where the crystallization processes occur and create a gas phase contact on the substate surface. These growth processes not only allow the thin films to grow layer-by-layer, but also give rise to very low intrinsic defects due to low momentum of the atoms or molecules. Meanwhile, as the gaseous sublimed atoms travel to the substrate, some gas molecules were introduced into the chamber to combine with the evaporated beams on the substrate surface in the crystallization zone. In Quantum Structures Lab, we use Zn, Mg, Cu, Cd and Ga sources in different effusion cells of SVTA customized build chamber, and for the gas molecules we use O_2. Before the O_2 is introduced into the chamber, the O_2 will flow through a radio-frequency plasma source which is controlled by needle valve and mass flow controller (MFC). The O_2 will be ionized to plasma state, this allows oxygen atoms much more easier to combine with

other atoms. MFC is connected between the oxygen gas cylinder and the RF plasma source, while the RF plasma source is connected to the MBE chamber directly. Before the growth, the wafer (substrate) which is placed on the holder is transferred from the load lock chamber into the main chamber. After the wafer and the holder are transferred into the main chamber, the holder is elevated to a specific growth height which is controlled by the manipulator. The wafer can be heated up to several hundred degree Celsius with the heater which is made of graphite, the temperature precision is 1 ˚C. In conclusion, MBE is an accurate and versatile technique for achieving high quality semiconductor thin film materials.

Figures

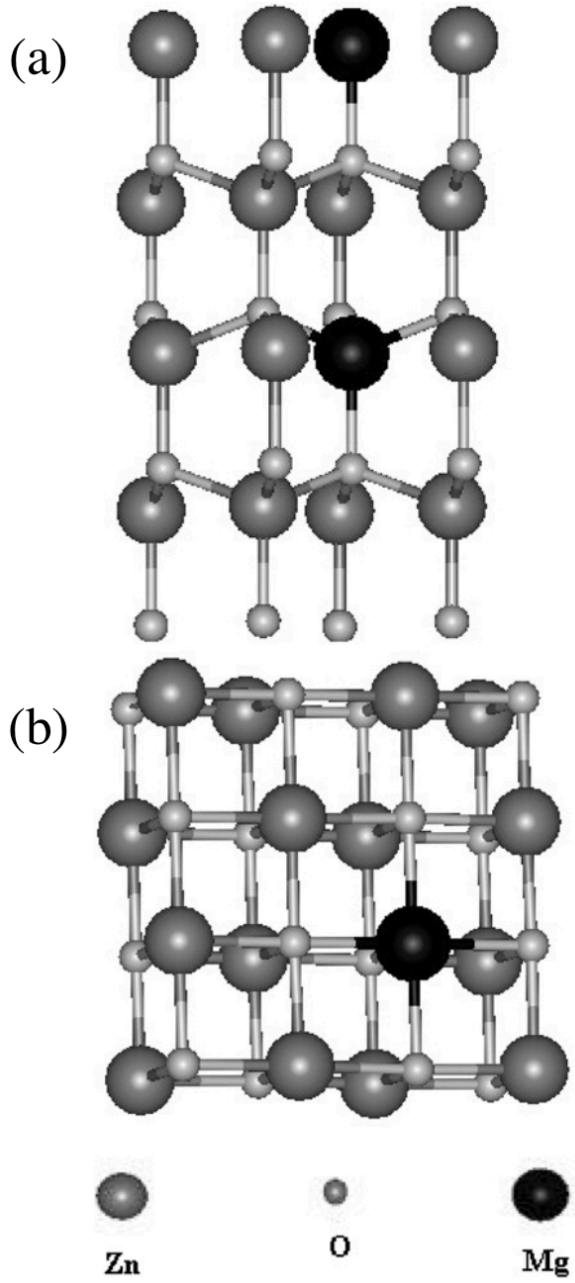

Figure. 1.1 The structure models of (a) hexagonal and (b) cubic MgZnO ternary alloy [9].

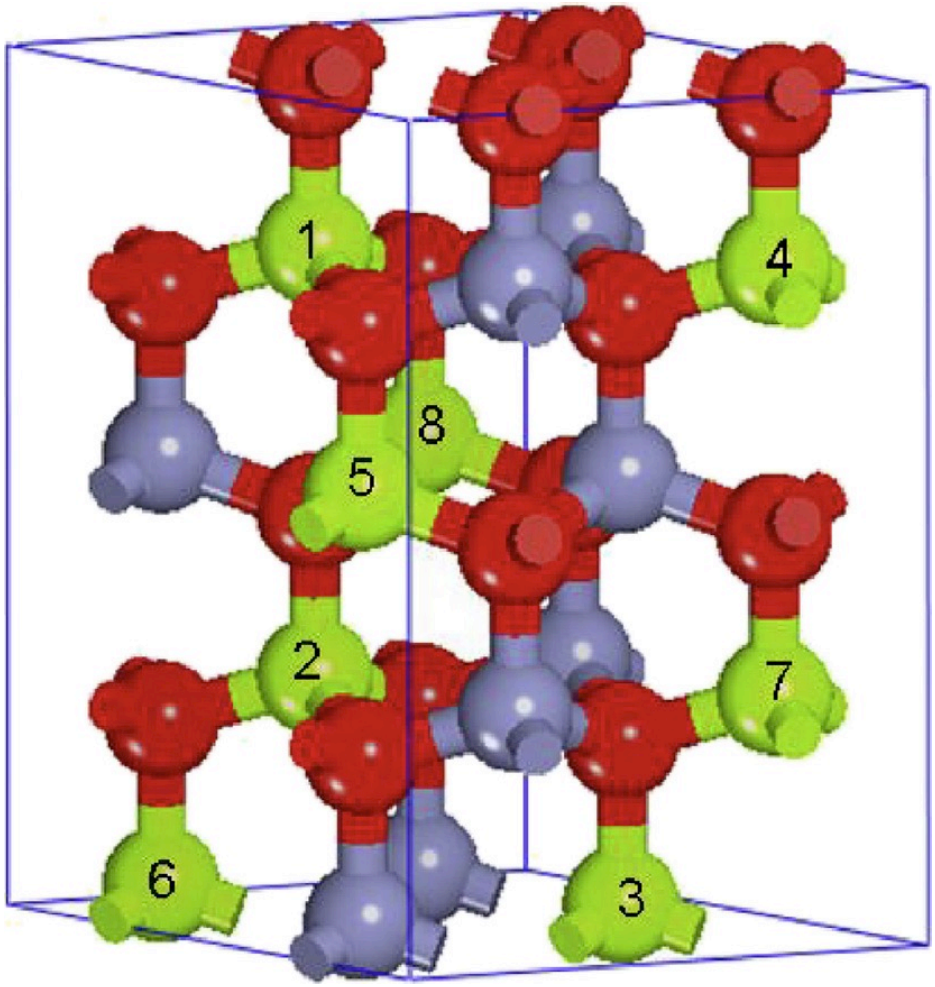

Figure. 1.2 The 2 × 2 × 2 hexagonal wurtzite ZnO supercell doped with Mg replacing the Zn position. Red, blue and green spheres represent O, Zn and Mg atoms respectively [10].

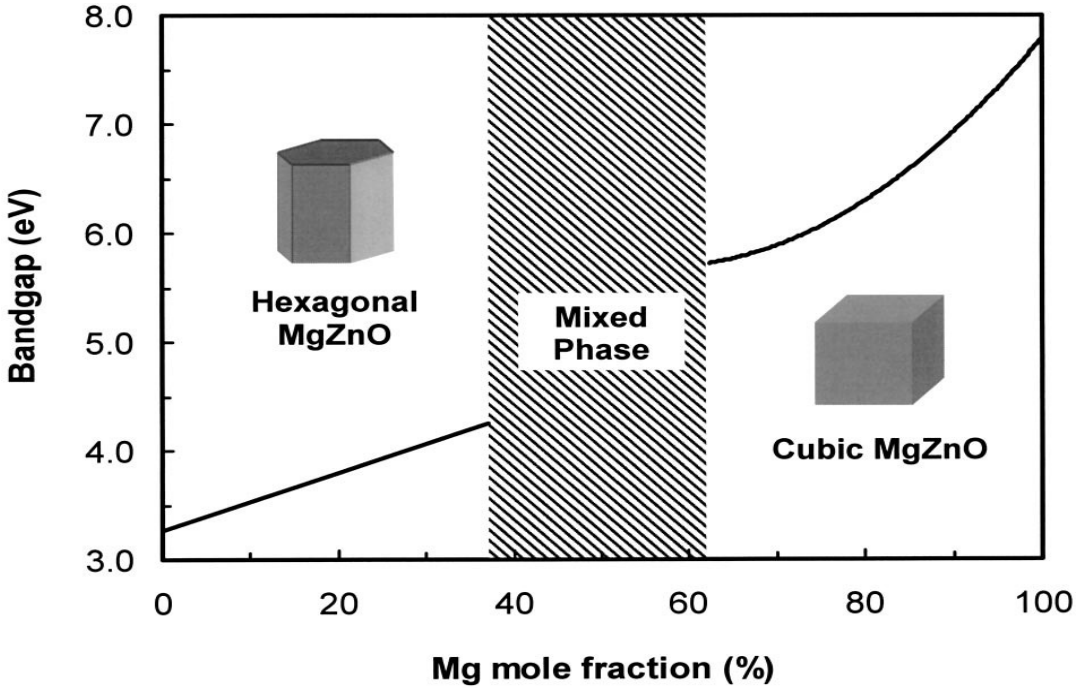

Figure. 1.3 The band-gap energy as a function of Mg content in $Mg_xZn_{1-x}O$ thin films [12].

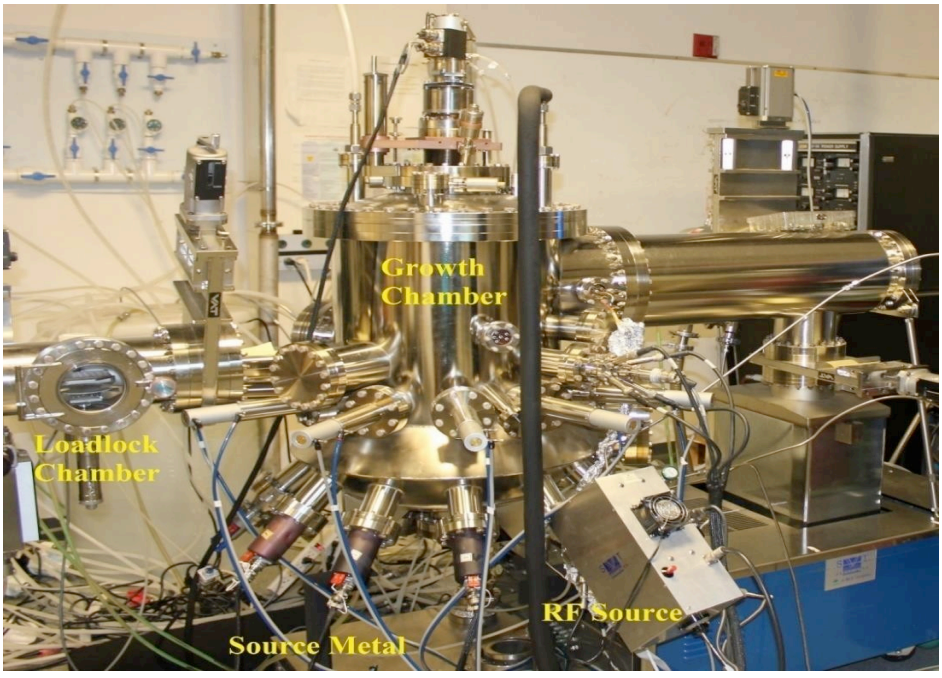

Figure. 1.4 Molecular beam epitaxy chamber in Quantum Structures Lab.

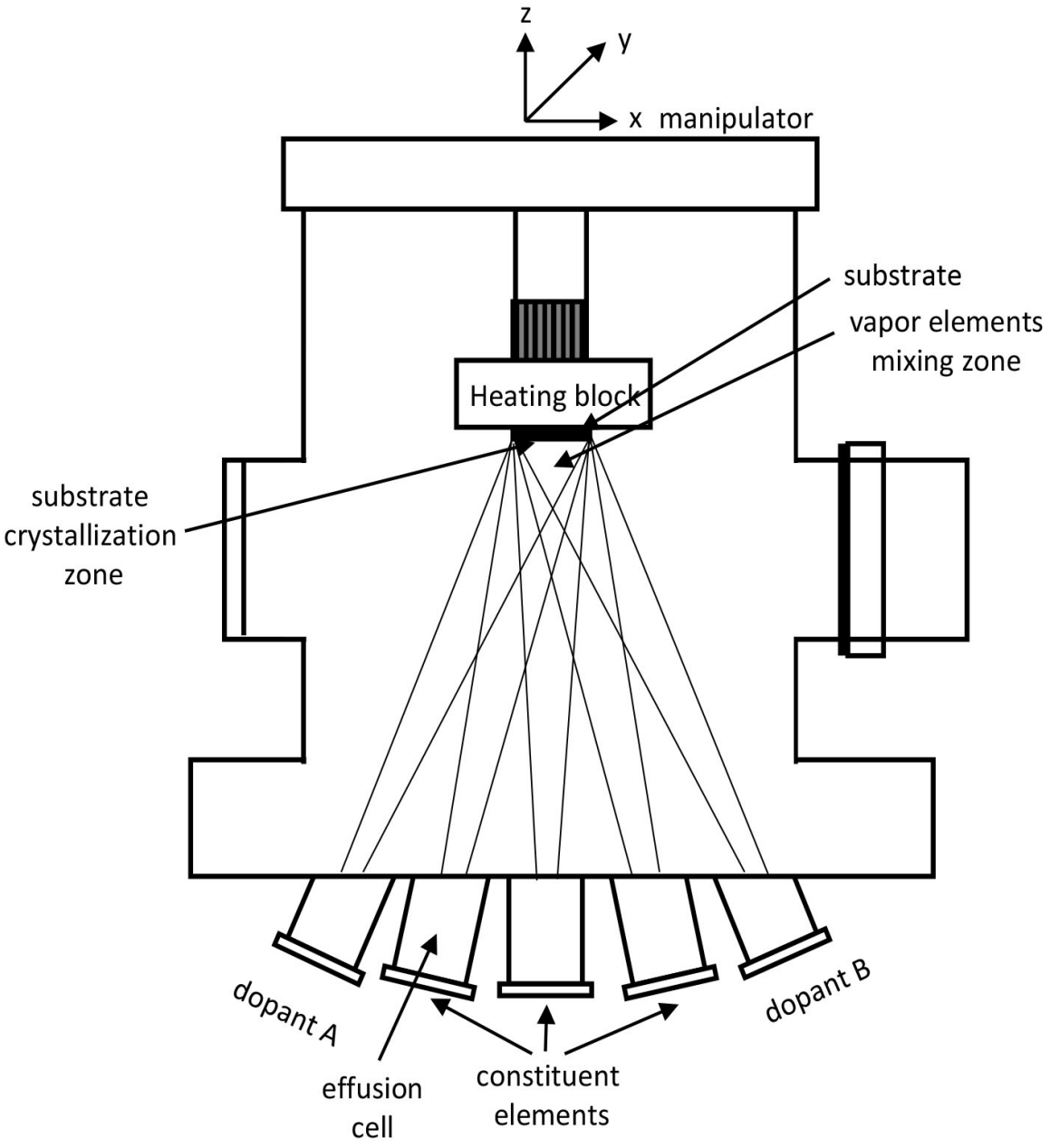

Figure. 1.5 Schematic of molecular beam epitaxy system in Quantum Structures Lab.

Table

Material	Structure	Lattice constants a (Å)	c (Å)	Bandgap at RT (eV)	Melting point (K)	Exciton binding energy (meV)
ZnO	wurtzite	3.249	5.207	3.37	2248	60
ZnS	wurtzite	3.823	6.261	3.8	2103	39
ZnSe	Zinc blende	5.668	—	2.70	1793	20
GaN	wurtzite	3.189	5.185	3.39	1973	21
6H-SiC	wurtzite	3.081	15.117	2.86 (ind)	>2100	—

Table. 1.1 Comparison of the properties of ZnO with other wide band gap semiconductor materials.

Impurity	Character	Ionization energy	n_{max} or p_{max} (cm^{-3})
Al	Donor	120 meV	8.0×10^{20}
Ga	Donor	—	1.1×10^{20}
In	Donor	—	3.7×10^{20}
F	Donor	80 meV	5.0×10^{20}
H	Donor	35 meV	—
Li	Acceptor	—	—
Cu	Acceptor	—	—
N	Acceptor	100 meV	9.0×10^{16}

Table. 1.2 Properties of different dopant impurities in ZnO. n_{max} or p_{max} shows the highest experimental carrier concentration.

Mg mole fraction	Lattice constant (Å)			
	Hexagonal $Mg_xZn_{1-x}O$ alloy		Cubic $Mg_xZn_{1-x}O$ alloy	
	a axis	c axis	a axis	c axis
0.0000	3.2682	5.3340	4.3300	4.3300
0.0625	3.2656	5.2941	4.3244	4.3208
0.125	3.263	5.2783	4.3188	4.3144
0.1875	3.2589	5.2764	4.3131	4.3118
0.25	3.2569	5.261	4.3075	4.3078
0.3125	3.2553	5.2498	4.3019	4.3027
0.375	3.2527	5.2446	4.2963	4.2965
0.4375	3.2501	5.2338	4.2906	4.2886
0.5	3.2475	5.2182	4.285	4.2879
0.5625	3.2449	5.2093	4.2794	4.2842
0.625	3.2424	5.2009	4.2738	4.2753
0.6875	3.2398	5.1774	4.2681	4.2691
0.75	3.2371	5.1623	4.2625	4.2642
0.8125	3.2325	5.1466	4.2569	4.2661
0.875	3.232	5.1293	4.2513	4.2565
0.9375	3.2294	5.0969	4.2456	4.2488
1	3.2268	5.0449	4.24	4.24

Table. 1.3 The calculated lattice constants of the hexagonal and cubic $Mg_xZn_{1-x}O$.

Chapter 2

ZnO and MgZnO thin film growth

2.1 ZnO thin film growth

In the past few decades, ZnO thin films were reported and studied very widely due to promising deep UV region applications. There are variety of growth methods to grow ZnO thin films such as pulsed laser deposition (PLD), metal organic chemical vapor deposition (MOCVD), molecular beam epitaxy (MBE) and so on. In our lab we use plasma-assisted MBE to achieve high quality ZnO thin films. ZnO thin film growths by plasma assisted MBE have been done and studied widely in the past few decades [1, 16-24]. Compared with other conventional synthesis methods, MBE provides the highest purity growth results and very precise control of thin films thickness. SiC and sapphire are the most adapted substrates for ZnO thin films growth in MBE system. Although SiC provides the better lattice mismatch than sapphire for ZnO growth, it is much more expensive than sapphire. Considering the commercial requirement, we use c-plane sapphire as the wafer for ZnO thin films growth. Figure 2.1 shows the schematic diagram showing the epitaxial relationship of ZnO (0001) grown on c-plane sapphire Al_2O_3 (0001) [1]. There are two different in-plane orientations between ZnO and c-plane sapphire which are ZnO[2 -1 -1 0]/ / Al_2O_3[1 -1 0 0] and ZnO[1 -1 0 0]/ / Al_2O_3[1 -2 1 0]. There is a 30° rotation between these two crystal orientations, the former has 18% of lattice mismatch while the latter has 32% of lattice mismatch. The reduction of lattice mismatch from 32% from 18% has been discovered by Chen et al [1]. The result of the former

orientation is because ZnO lattice aligns itself with the oxygen sublattice in Al_2O_3. This can be achieved with oxygen plasma pre-treatment by exposing the substrate surface to energetic atomic oxygen. A further research shows that the surface morphology of ZnO grown on c-plane sapphire can be improved by inserting a MgO buffer layer between ZnO and sapphire [25]. The wafer we use for the ZnO thin film growth is one-side polish c-plane sapphire and the Knudsen cells are used with 6N purity of zinc and 3N purity of magnesium source. Before the growth, the sapphire is cleaned by the ultrasonic cleaner with the mixture ratio 1:1 of water and isopropanol for 5 minutes. After the cleaning process, the sapphire is washed with deionized water and dried by the nitrogen inside the compressed cylinder. Then the wafer is placed in the load lock and transferred into the main chamber after being pumped by mechanical pump and molecular pump for more than 6 hours. The wafer is transferred into main chamber and mounted to a specific heigh and is ready for growth. Figure 2.2 shows the growth procedure of ZnO thin film. At the beginning of the growth, the wafer is heated from room temperature to 800 ˚C holding for 10 minutes then cooled down to 450 ˚C (buffer layer growth temperature). By the pre-growth thermal treatment process, the surface of sapphire becomes smoother, which is qualified to be good nucleation sites for ZnO film growth. Before the deposition of ZnO active layer, a very thin bi-layer buffer (only several nanometers) composed of MgO layer grown for 1.5 minutes and ZnO layer grown for 3.5 minutes is inserted between c-plane sapphire and ZnO active layer to improve the surface morphology. Meanwhile, the RF plasma is ignited with the power of 400W and the cell temperature is increased to

desired temperature. Then the active epitaxial layer of ZnO is grown for 2 hours at desired temperature, here we use 300 ˚C. The oxygen flow for active layer growth is 2.5 sccm. Finally the post annealing is carried out at 700 ˚C holding for 20 minutes. All the process above are under oxygen ambient condition.

2.2 MgZnO thin film growth

MgZnO ternary alloy is one of the wider band gap ZnO based semiconductor materials that has raised most interests among researchers due to the promising deep ultraviolet applications. The band gap widening engineering of ZnO thin films by incorporating Mg have been published prevalently recently [26-31]. By incorporating Mg into ZnO, the band gap can be tuned from 3.37 eV to 7.8eV. The largest issue of ZnO alloying with Mg is the phase separation. The MgZnO alloy can remain single hexagonal wurtzite crystal structure when the Mg content is below 33%, while the mixed phase structure of wurtzite and cubic emerge once the Mg content exceed 33%. Figure 2.3 shows the growth procedure of MgZnO thin film. Basically the procedure is identical to the ZnO thin film growth. However, the buffer layer plays a significant role in MgZnO ternary alloy growth. The buffer layer which is inserted between sapphire and MgZnO ternary alloy reduces not only the lattice mismatch but also the structural defects. By controlling the thickness ratio of MgO and ZnO will significantly affect the growth of active layer. To achieve high quality thin films, we introduce a buffer layer annealing process to further improve the crystal quality. After the deposition of the bi-layer buffer, the buffer layer is annealed from 450 ˚C to 650 ˚C holding for 5 minutes then cooled down to 300 ˚C (active

layer growth temperature). By this thermal treatment, the atomic rearrangement took place and the defects of thin films are reduced [32].

2.3 Sample characterization methods

The samples are characterized by different methods to evaluate their optical, structural and electrical properties. For the photoluminescence optical property, we use Oriel photoluminescence system with a Kimmon Koha He-Gd 325 nm (ultraviolet light) and 442 nm (blue light) laser excitation sources to measure the PL spectrum. Here we use 325 nm light source for the thin film characterization, the range of the characterized wavelength is from 320 nm to 600 nm. Figure 2.4 shows the schematic diagram of a PL measurement system set-up. First the laser source emits through a optical chopper which is connected to lock-in amplifier. By the frequency rotating chopper, the intensity of light beams can be modulated. After the light beams emits through the chopper, it is reflected by a mirror and directly shines on the sample. Then the spontaneous light emission from the sample will go through two biconvex lenses parallel to each other. The focused spontaneous light will shine into a monochromator, which is connected to a light detector. Finally the emission light will be received by lock-in amplifier which is used to improve the signal-to-noise ratio. For the absorption optical property, we use Agilent Cary500 UV-Vis spectrophotometer. The range of the characterized wavelength is from 190 nm to 600 nm. For the structural property we use PANalytical Empyrean Series 2 to obtain the XRD spectrum.

Figures

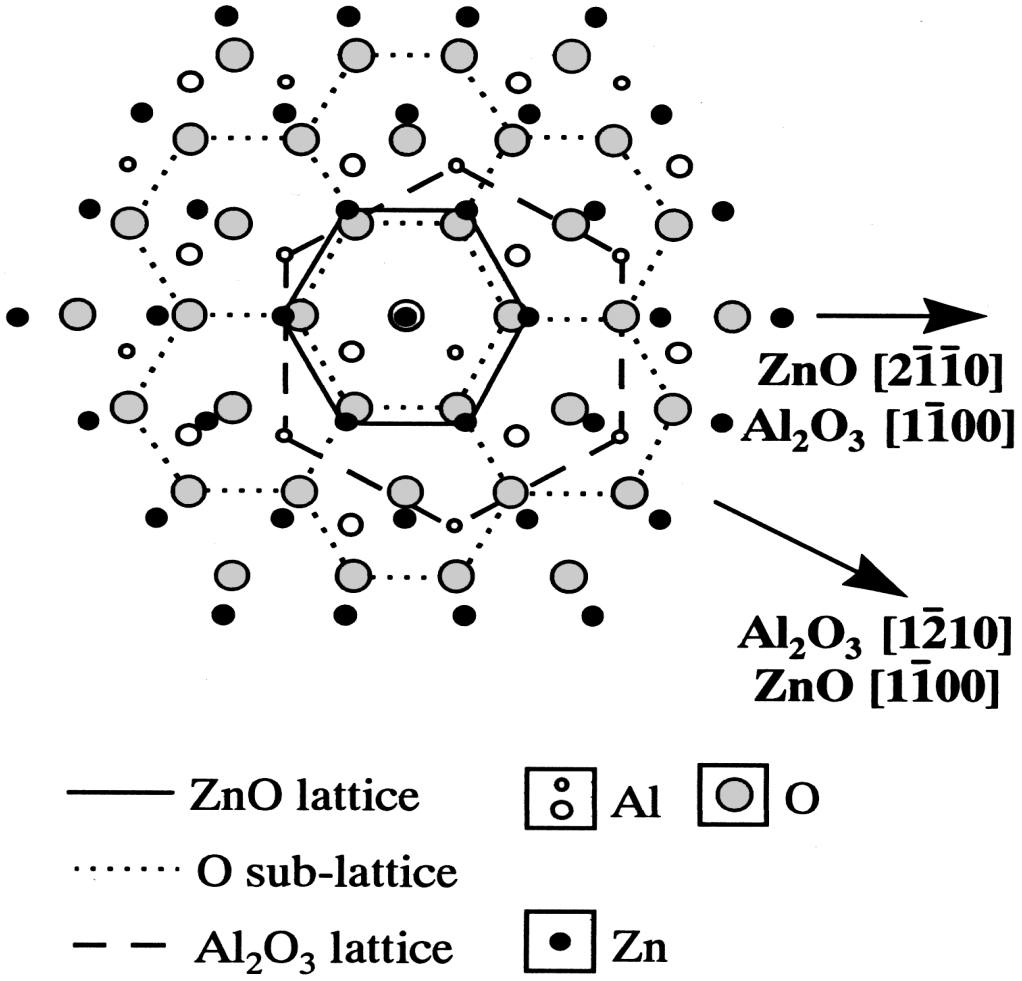

Figure. 2.1 Schematic diagram showing the epitaxial relationship of ZnO (0001) grown on c-plane sapphire Al_2O_3 (0001) [1].

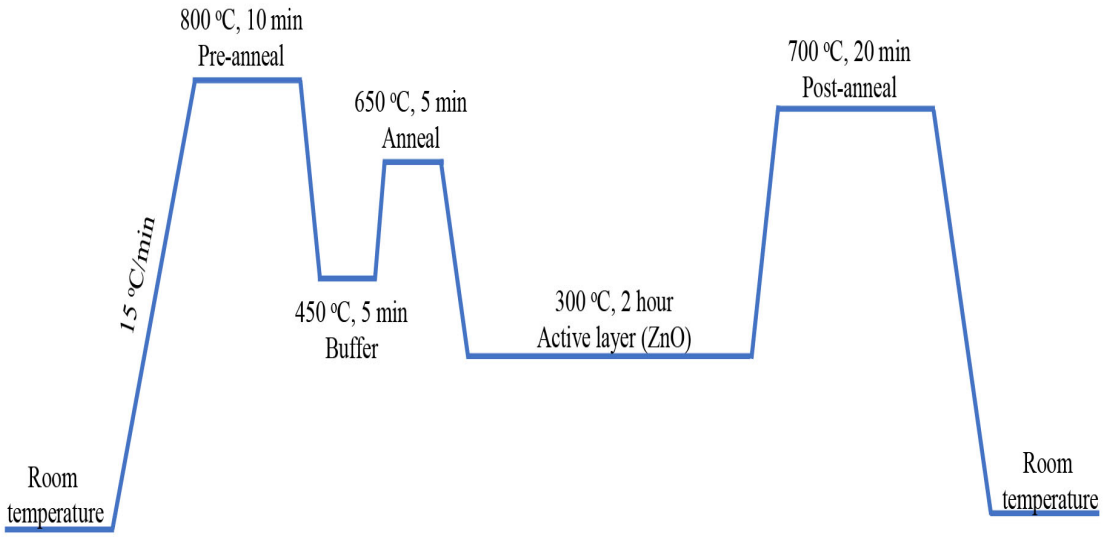

Figure. 2.2 Growth procedure of ZnO thin film.

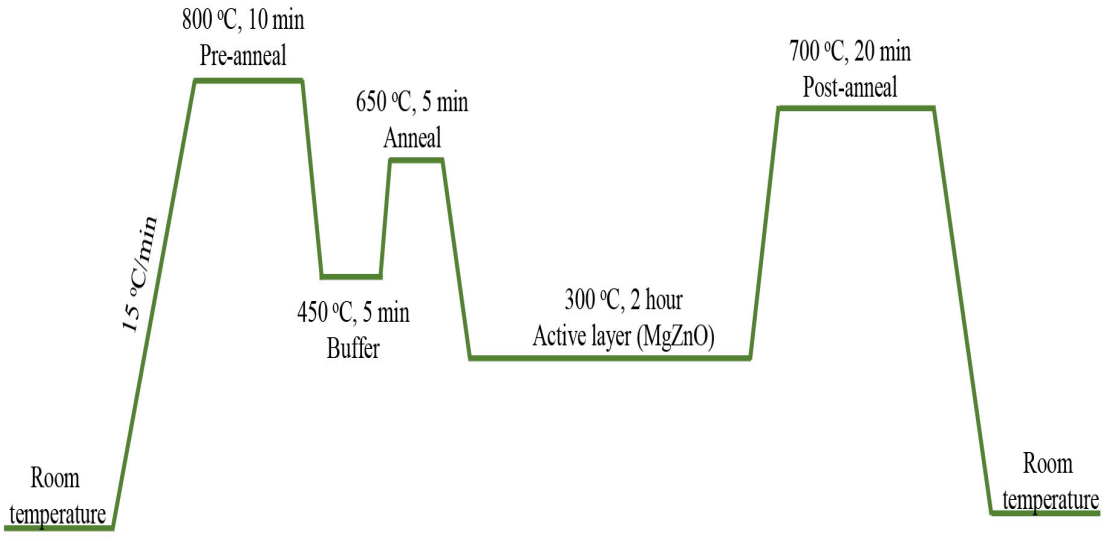

Figure. 2.3 Growth procedure of MgZnO thin film.

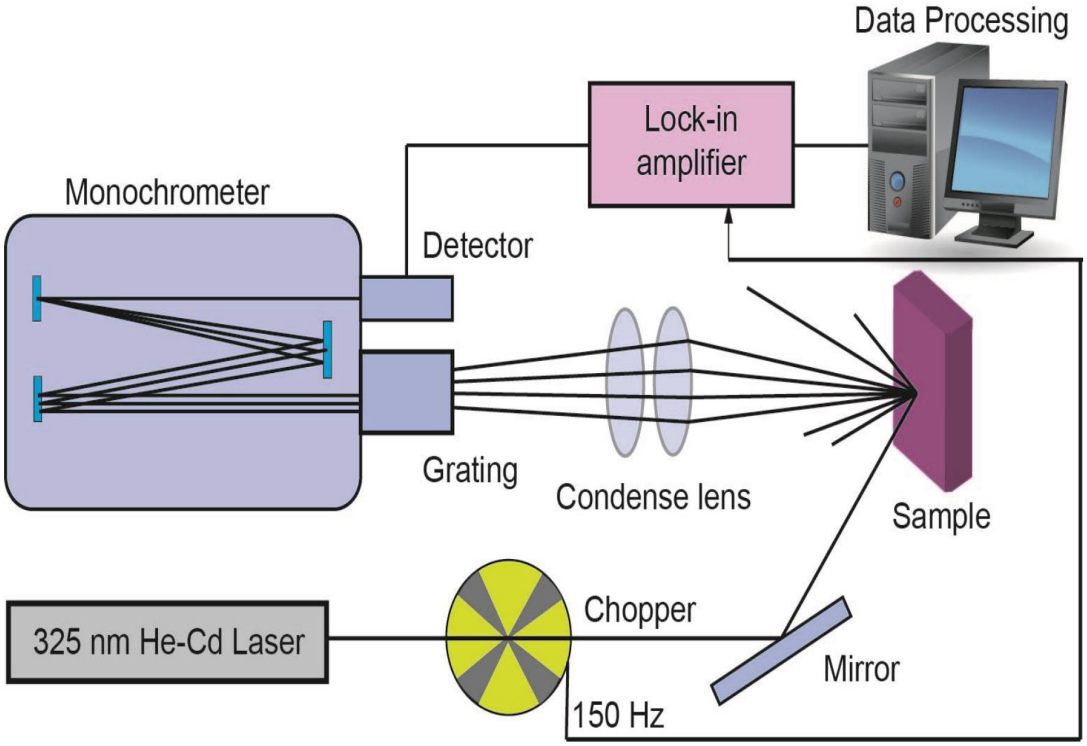

Figure. 2.4 Schematic diagram of a PL measurement system set-up.

Chapter 3

ZnO and MgZnO thin film characterization

3.1 ZnO thin film characterization

ZnO is one of the most popular semiconductor materials due to its UV region band gap energy of 3.37 eV and high binding energy of 60 meV. It is necessary to study ZnO thin films before investigating MgZnO ternary alloy. As a promising optoelectronic semiconductor material the optical and electrical properties are very important, here we study the photoluminescence (PL), absorption, X-Ray diffraction (XRD) and Hall effect of ZnO thin films. The sample was heated from room temperature to 800 ˚C before the growth. After annealing, a bi-layer buffer of MgO and ZnO is deposited under 450 ˚C on the sapphire, which is grown with 1.5 minutes (Zn cell at 305 ˚C) and 3.5 minutes (Mg cell at 450 ˚C), respectively and the oxygen flow of 1.5 sccm. Then a buffer annealing took place in order to increase the epitaxial layer quality. After the growth of the buffer layer, the active layer is grown with substrate temperature at 300˚C and Zn cell temperature at 305 ˚C and oxygen flow of 2.5 sccm. After the active layer is grown, a post-annealing process is used to further improve the crystal quality. There are two ZnO thin films grown with above conditions, where sample A was annealed with oxygen ambient and sample B was annealed without oxygen ambient.Table 3.1 shows the growth condition of 2 ZnO samples annealed with (A) and without (B) oxygen ambient. Figure 3.1.1 shows the PL spectrum of sample A and sample B. The emission peaks of both sample A and B are located at ~380 nm which is corresponding to 3.26 eV, however, this

emission peak has ~0.11 eV shift from the band gap energy of 3.37 eV at room temperature due to the temperature effect. Figure 3.1.2 shows the temperature dependent PL of ZnO from 4.8 K (a) to 290 K (g) [33]. At 4.8 K, the emission peak is dominated by bound-exciton (BX) near 3.36 eV which is very close to the band gap energy 3.37 eV. As the temperature increases, the bound-exciton peak starts to separate from free-exciton (FX) which was observed at 3.37 eV at 4.8 K. Then the free-exciton peak gradually shifts closer to first longitudinal-optical (LO) phonon peak, which was observed at 3.3 eV at 100 K. Finally, the free-exciton peak and the first longitudinal-optical phonon peak merge with each other at room temperature with an emission peak at 3.26 eV, corresponding to 380 nm. Furthermore, from figure 3.1.1 we can observe another peak of sample B at ~500 nm. This green luminescence peak is considered the native point defect peak of ZnO caused by the electronic transitions between shallow donors and deep acceptors (V_{Zn}) [34-36]. Figure 3.1.3 shows the absorption spectrum of sample A and sample B. Both the absorption edges of sample A and B are located at 379 nm which are very similar to the PL emission peaks. Figure 3.1.4 shows the Tauc plot of both A and B samples. The x-axis represents the energy hν and the y-axis represents the quantity (αhν)^(1/r), where α is the absorption coefficient (α = 2.303*absorbance of the absorption spectrum) and r is the nature of the transition (here we use r = 1/2 for direct allowed transitions). From Tauc plot we can calculate the band gap of the material by the intersection between the extending tangent of the Tauc plot curve with the largest slope and the x-intercept. From Tauc plot we can determine the band gap of 3.29 eV for both

sample A and B. Figure 3.1.5 shows the XRD spectrum of sample A and B. A (002) single wurtzite peak can be observed at ~34.6˚ for both sample A and B. Table 3.2 shows the above characterization results of both sample A and B.

3.2 MgZnO thin film characterization

As one of the ZnO based semiconductor materials, the characterization of MgZnO ternary alloy is very important for determining the thin film properties. Recently, many researches which carried out MgZnO thin film growth have done variety of characterizations such as photoluminescence, absorption, X-ray diffraction and so on. However, very few of them study the results that affect the Mg incorporation of ZnO under different growth condition. Here we will investigate how the growth conditions influence the MgZnO thin films. The goal we are focusing on is single wurtzite MgZnO thin films, in other word, without phase separation. First of all, single-crystalline thin films have better performance than mix-phase thin films as the material of fabricating optoelectronic devices. Furthermore, a direct to indirect band gap transition is observed for MgZnO when Mg concentration is higher than atomic percentage of 75 % [37]. Therefore, the main purpose in this thesis is synthesizing single wurtzite MgZnO ternary thin films.

3.2.1 Growth temperature

Growth temperature also known as substrate temperature, is the most important experimental parameter for the epitaxial growth. Temperature has significant influence on

different atomic processes such as adsorption, desorption, surface adatom diffusion, bulk diffusion, dislocation motion, migration and impurity segregation since they are all thermally activated. Figure 3.2.1 shows a series of surface processes of thin film growth : (i) the adsorption of the evaporated atoms or molecules, (ii) the surface migration and dissociation of the adsorbed molecules, (iii) the incorporation of the constituent atoms into the crystal lattice of the substrate surface or the epilayer, (iv) thermal desorption of the adatoms not crystalized into the crystal lattice [15]. The balance of the surface thermal processes will decide how the epitaxial layer is grown, therefore growth temperature is the most critical condition for thin film growth. In general, higher temperatures lead to more mobile surface atoms and thus more highly ordered material. The disadvantage is that inter-diffusion on the interfaces become more severe due to diffusion of atoms. On the other hand, lower temperatures generate more abrupt interfaces, which usually have better quality, however, the lower mobility of atoms lead to more point defects for the layer. Adopting a proper substrate temperature for the thin film growth is a very important task for the MBE growers, different materials have different growth temperature range. If the growth temperature is lower than a specific temperature, the deposited film will no longer be crystallized. The limit of the high temperature is defined by the balance between the processes of adsorption and desorption, in other word, the equilibrium of thermodynamic phase. In the past few decades, the substrate temperature of MgZnO thin film grown by MBE has a wide temperature range from around 300 ˚C to 500 ˚C or even higher. In this thesis, we use the

substrate temperature from 270 ˚C to 500 ˚C. The samples were heated from the room temperature to 800 ˚C before the growth. After annealing, a bi-layer buffer of MgO and ZnO deposited under 450 ˚C on the sapphire is grown with 1.5 minutes and 3.5 minutes individually and the oxygen flow of 1.5 sccm. Then a buffer annealing took place in order to increase the epitaxial layer quality. After the buffer layer is deposited, the active layer is grown with substrate temperature at 280˚C, 300 ˚C, 350 ˚C and 450 ˚C, respectively with Zn cell temperature at 285 ˚C, Mg cell temperature at 450 ˚C and oxygen flow of 2.5 sccm. Table 3.3 indicates the growth conditions of these 4 samples. After the active layer is grown, a post-annealing is used to further improve the crystal quality. Figure 3.2.2 shows the PL spectrum of sample 1-4 grown with substrate temperature at 280 ˚C, 300 ˚C, 350 ˚C and 450 ˚C respectively. Sample 1 and 2 have the emission peak at 360 nm and 358 nm, respectively while sample 1 has an impurity-vacancy complex peak at 420 nm and sample 2 has a green luminescence peak of ZnO at 500nm, which is caused by the V_{Zn}. On the other hand, both sample 3 and 4 don't have a relatively weak emission peak at 360 nm but a very strong impurity-vacancy complex peak at 410 nm. In this case, the peak at ~360 nm can not be considered as emission peak associated with band gap. The reason is that the laser we used is 325nm, the material can not be measured if the band gap is much larger than 3.8 eV (325nm). Moreover, the intensity of the PL spectrum can further reveal the thickness of the thin film. As the substrate temperature increases, the intensity decreases, in other words, the thickness is also decreased. The result indicates that the desorption rate is larger than the adsorption rate as the substrate temperature

keeps increasing. We can also learn from the Polanyi-Wigner equation that the desorption rate of the surface adatoms increases while the substrate temperature increases [38, 39]. Therefore, the thickness of the thin film decreases as the substrate temperature increases. Figure 3.2.3 shows the absorption spectrum of 4 samples grown with different substrate temperature. As seen from the absorption spectrum, the absorption edges have blue shift from 310 nm to 230nm as the substrate temperature increases. The result indicates that the thin films have higher Mg incorporation grown with higher substrate temperature. In other words, from the previous discussion we can postulate that ZnO has higher desorption rate than MgO grown on c-plane sapphire as the substrate temperature is elevated. Furthermore, for sample 1, 3 and 4 we can clearly observe a weak absorption tail at longer wavelength. A study indicated that the weak absorption tail is caused by the defect-induced absorption, which is corresponding to the impurity-vacancy complex peak of PL spectra for sample 1, 3 and 4 [40]. Figure 3.2.4 shows the Tauc plot of these 4 samples. From the figure we can further prove that the thin films have higher MgO content as the substrate temperature increases, the results are shown in Table 3.4. By equation 1 we can approximately calculate the Mg concentration of sample 1-3 with 25.8%, 29.6%, 37.3%, respectively, the equation is not applicable for sample 4 because the band gap is larger than 4.28 eV. Figure 3.2.5 shows the XRD spectrum of sample 1-4. The relatively strong peak which is located at deflection angle (2θ) ~42˚ is the (006) plane of the sapphire (Al_2O_3) substrate. For sample 1-3 we can observe a peak ~35˚ which indicates the (002) plane of ZnO with wurtzite structure. Those peaks have

approximately 0.4˚-0.5˚ shift compared with that of pure ZnO which is located at 34.68˚. According to Bragg's law :

$$2dsin\theta = n\lambda$$

(d is the spacing between diffracting planes, θ is the incident angle, n is any integer, and λ is the wavelength of the beam) we know that as the lattice constant decreases the deflection angle increases. Since the lattice constant of MgZnO decreases as the Mg incorporation increases (see Table 1.3), the deflection angle will also increase. If we take a look at the zoom-in of Figure 3.2.4 we can observe a 0.08˚ peak shift from 35.075˚ to 35.155˚ of sample 2 and 3. It can further verify that the thin films have higher Mg incorporation as the substrate temperature increases. However, the peak of sample 4 is shifted to 37.005˚ which is the (100) plane of cubic MgO. In other word, the MgZnO ternary alloy is dominated by MgO instead of ZnO. Table 3.4 shows the above characterization results of sample 1-4.

3.2.2 Effusion cell temperature

Effusion cell temperature or source temperature is another important parameter of epitaxial layer growth. Compared with substrate temperature, substrate temperature affects diffusive properties of impinging atoms such as adsorption, migration, desorption and so on, whereas the cell temperature affects the speed of impinging atoms, namely, the flux rate. Higher effusion cell temperature can increase the velocity of impinging atoms

thus lead to thicker thickness of the thin film. Furthermore, changing the effusion cell temperature can also affect the flux ratio especially for alloying growth. Typically the effusion cell temperature for growth is dictated by the flux of material required and the melting point of the materials. For instance, the melting point of Zn is 419 ˚C and Mg is 649 ˚C, but the operating required temperature is around 250 ˚C and 327 ˚C for Zn and Mg, respectively. Operating with or higher than required temperatures can achieve a suitable flux for the thin film growth. In this thesis we study how the effusion cell temperature affects the Mg incorporation into ZnO. Table 3.5 shows the growth conditions of 4 different samples grown with different Zn cell temperatures, while other growth conditions such as substrate temperature, buffer layer, oxygen flow and annealing temperature are identical. The substrates were heated from room temperature to 800˚C before the growth. Then a bi-layer buffer of MgO and ZnO is deposited under 450 ˚C on the sapphire, which is grown with 1.5 minutes and 3.5 minutes individually and the oxygen flow of 1.5 sccm. Then a buffer annealing took place in order to increase the epitaxial layer quality. After the buffer layer is deposited, the active layer is grown with 305 ˚C, 295 ˚C, 285 ˚C and 275 ˚C of Zn cell temperature, respectively, the Mg cell temperature at 450 ˚C, substrate temperature at 300 ˚C, and oxygen flow of 2.5 sccm. After the active layer is grown, a post-annealing is occurred to further improve the crystal quality. Here we adjust Zn cell temperature while maintain the same Mg cell temperature because we want to compare the results with only one independent variable. Moreover, the change of Mg incorporation will be more rapidly by adjusting Zn cell temperature

because MgZnO is ZnO based alloy. Figure 3.2.6 shows the PL spectra of the 4 samples grown with different Zn cell temperature. For both sample 5 and sample 6, the emission peaks are located at ~365 nm. As the Zn cell decreases from 305 ˚C (sample 5) to 285 ˚C (sample 2), the peak shifts to 358 nm. The result is reasonable because of the lower impinging speed of evaporated Zn atoms, in other words, the partial pressure of Zn flux is decreased. Thus, it allows more Mg atoms incorporating into ZnO. When the Zn cell temperature further decreases to 275 ˚C (sample 7), the emission peak is vanished because the band gap energy is higher than the energy of incident laser photon which is 3.82 eV (325 nm). Instead, an impurity-vacancy complex peak is located at 400 nm. Figure 3.2.7 shows the absorption spectra of these 4 samples. We can observe a very large peak-shift from 342nm (sample 5) to 219 nm (sample 7) as the Zn cell temperature decreases. Figure 3.2.8 shows the Tauc plot of these 4 samples, the band gap energies are shown in Table 3.6. By applying the band gap to equation 1 we can approximately calculate the Mg content of sample 5,6 and 2 with 15.5%, 19.7% and 29.6% respectively, the equation is not applicable for sample 7 because the band gap is larger than 4.28 eV. Figure 3.2.9 shows the XRD spectra of these 4 samples. For sample 5, 6 and 2 we can observe a (002) single wurtzite peak at ~ 35˚. If we look at the zoom-in figure of Figure 3.2.9 we can observe a ~0.2˚ peak shift from sample 5 to sample 2. For sample 7, the intensity of the (002) wurtzite peak at ~35˚ decreases rapidly, instead, a peak at ~42˚ emerges which is (200) plane of cubic MgO. Comparing the Zn cell temperature series with the substrate temperature series of MgZnO thin films, sample 7 has (200) MgO

cubic plane while sample 4 has (111) MgO cubic plane. At Mg concentration around 0.45, the (111) peak starts to develop, and the intensity saturates at Mg concentration around 0.6. As the Mg concentration is larger than 0.6, a (200) peak starts to emerge [41]. This result can further verify by the band gap of sample 7 and sample 4 which is 6.13 eV ($x > 0.6$) and 5.83 eV ($0.45 < x < 0.6$), respectively. Table 3.6 shows the above characterization results of sample 2, 5, 6 and 7.

3.2.3 Buffer layer

Buffer layer is a very crucial growth condition for the MBE thin growth. For the MBE thin film growth, lattice mismatch usually emerges between the epilayer and the substrate surface due to different lattice constants and the crystal structures. Inserting a buffer layer between epilayer and substrate can not only release the stress but also affect on the incorporation content. For the ZnO thin film grown on c-plane sapphire, the lattice mismatch is ~18%. Inserting a MgO buffer layer can further reduce the lattice mismatch to ~8% between MgO buffer layer and c-plane sapphire, and the lattice mismatch of ZnO epitaxial layer is reduced to half [25]. Three different epitaxial growth modes can take place between the substrate surface and the atoms which depend on the interaction strength between adatoms and the surface, in other words, the substrate temperature. The first mode is called Volmer–Weber (VW), which is 3D island formation. The second mode is called Frank–van der Merwe (FM), which is 2D layer-by-layer formation. The last mode is called Stranski–Krastanov (SK), which is 2D-3D transition mode. For

Stranski–Krastanov mode, transition from the layer-by-layer (2D) to island-based (3D) growth emerges at a critical thickness which is mostly depending on the chemical and physical properties such as surface energies and lattice parameters of the substrate and film. It has been found that MgO layer grown on c-plane sapphire by plasma-assisted molecular beam epitaxy follows the Stranski–Krastanov growth mode [42]. Adopting the 2D-3D transition phenomenon of MgO layer grown on sapphire can change the polarity of ZnO. ZnO has an unipolar behavior of either Zn-polar or O-polar while grown on c-plane sapphire. However, ZnO usually has O-polar while grown by plasma-assisted molecular beam epitaxy due to the O-terminated surface by the plasma surface treatment. Kato et al. found that controlling the MgO buffer layer thickness of ZnO thin film growth can switch the polarity, the critical thickness is ~2 nm [42]. In this section we will look into the characterizations of MgZnO thin films grown with different buffer layer. Table 3.7 shows the growth conditions of 3 samples grown with different buffer layer. The substrates were heated from room temperature to 800 ˚C before the growth. Then a single layer MgO buffer, single layer ZnO buffer and MgO/ZnO bi-layer buffer was deposited under 450 ˚C on the sapphire, which is grown with 1.5 minutes, 3.5 minutes and 5 minutes individually, and the oxygen flow of 1.5 sccm. Then a buffer annealing took place in order to increase the epitaxial layer quality. After the buffer layer is deposited, the active layer is grown with Zn cell temperature at 285 ˚C, Mg cell temperature at 450 ˚C, substrate temperature at 300 ˚C and oxygen flow of 2.5 sccm. After the active layer is grown, a post-annealing is used to further improve the crystal quality. Figure 3.2.10

shows the PL spectra of sample 8 (1.5 minutes MgO single layer buffer), sample 9 (3.5 minutes ZnO single layer buffer) and sample 2 (5 mins MgO/ZnO bi-layer buffer). Their emission peaks are all located at ~360 nm. However, only sample 9 has a very strong impurity-vacancy complex peak at 420nm, the defects peak of sample 8 and sample 2 are both vanished. The defect peak emerges because of the polarity of the thin films. As mentioned before, inserting MgO buffer layer can change the ZnO polarity from O-polar to Zn-polar, therefore, sample 2 and sample 8 have Zn-polar while sample 9 has O-polar. However, Zn-polar ZnO has smooth two-dimensional growth while O-polar has rough three-dimensional island growth [43]. Therefore, O-polar ZnO will generate much more point defects than Zn-polar, which lead to the strong impurity-vacancy complex peak. Figure 3.2.11 shows the absorption spectra of these 3 samples. All the 3 samples have similar absorption edge which is located at 317 nm. Figure 3.2.12 shows the Tauc plot of these 3 samples. All of them have the same band gap energy of ~4.05 eV, by inserting the band gap to equation 1 we can calculate the Mg concentration of 30%. From the above results we know that the buffer layer barely affect on Mg incorporation, instead, it affects on the native defects due to the switching of polarity. Figure 3.2.13 shows the XRD spectra of these three samples grown with different buffer layer. All three samples have deflection angle with ~35.1˚ which is (002) plane of wurtzite ZnO. Table 3.8 shows the above characterization results of sample 2, 8 and 9.

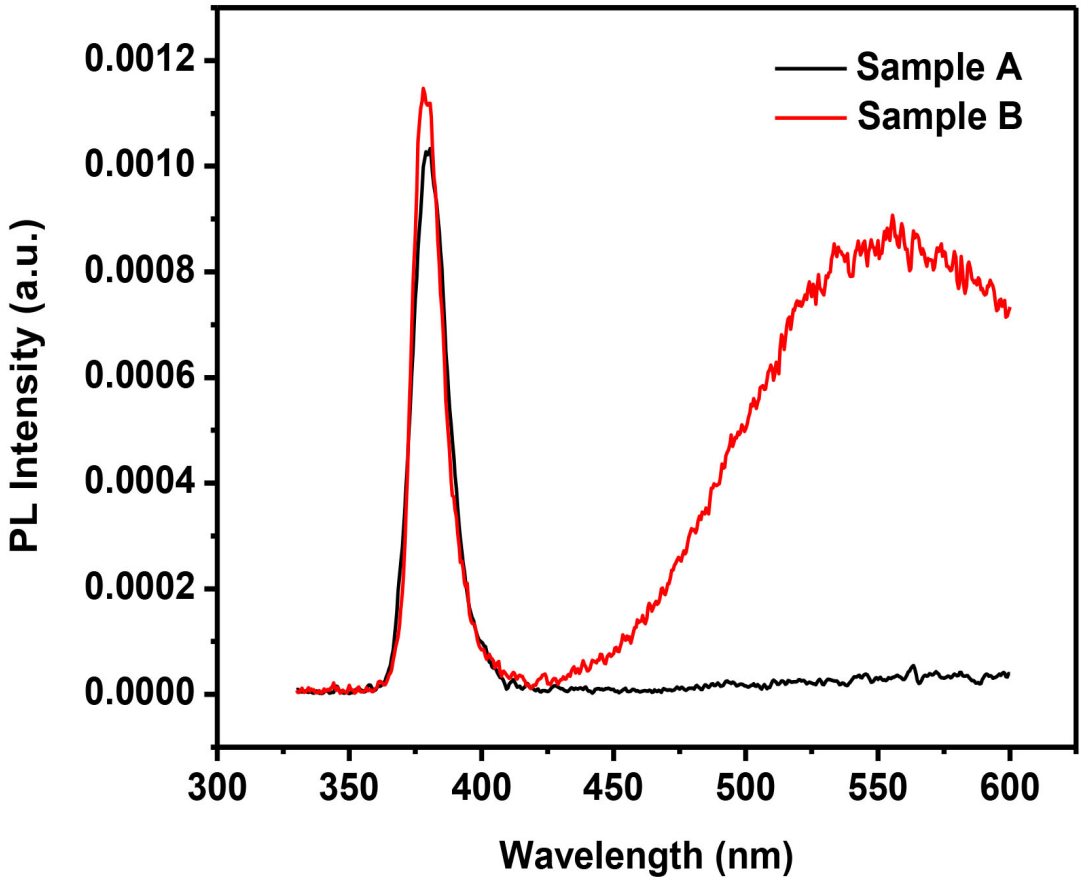

Figure. 3.1.1 PL spectrum of the ZnO samples annealed with (A) and without (B) oxygen ambient.

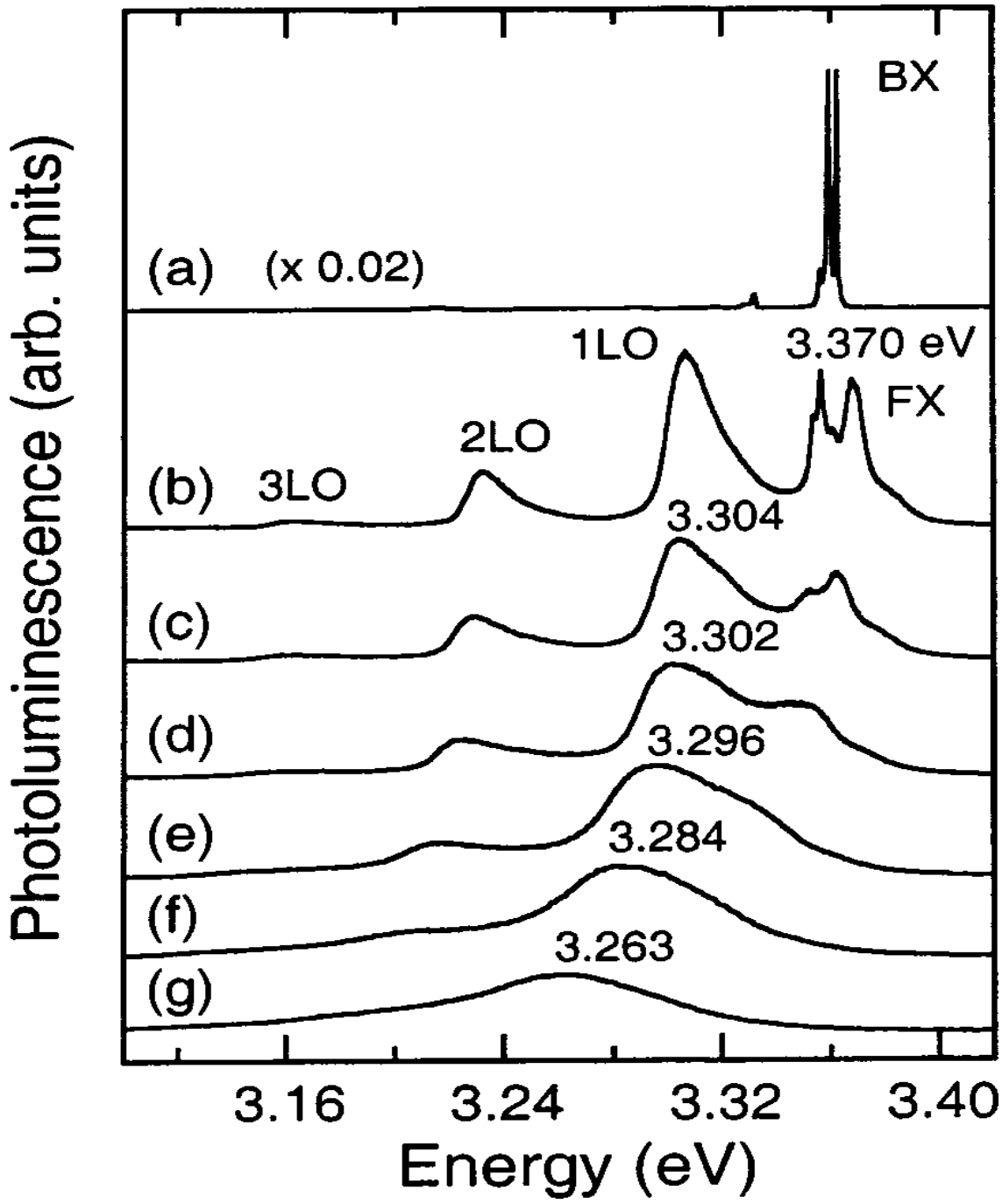

Figure. 3.1.2 Temperature dependent PL of ZnO. (a) 4.8 K, (b) 100K, (c) 130K, (d) 160 K, (e) 200 K, (f) 240 K and (g) 290 K [33].

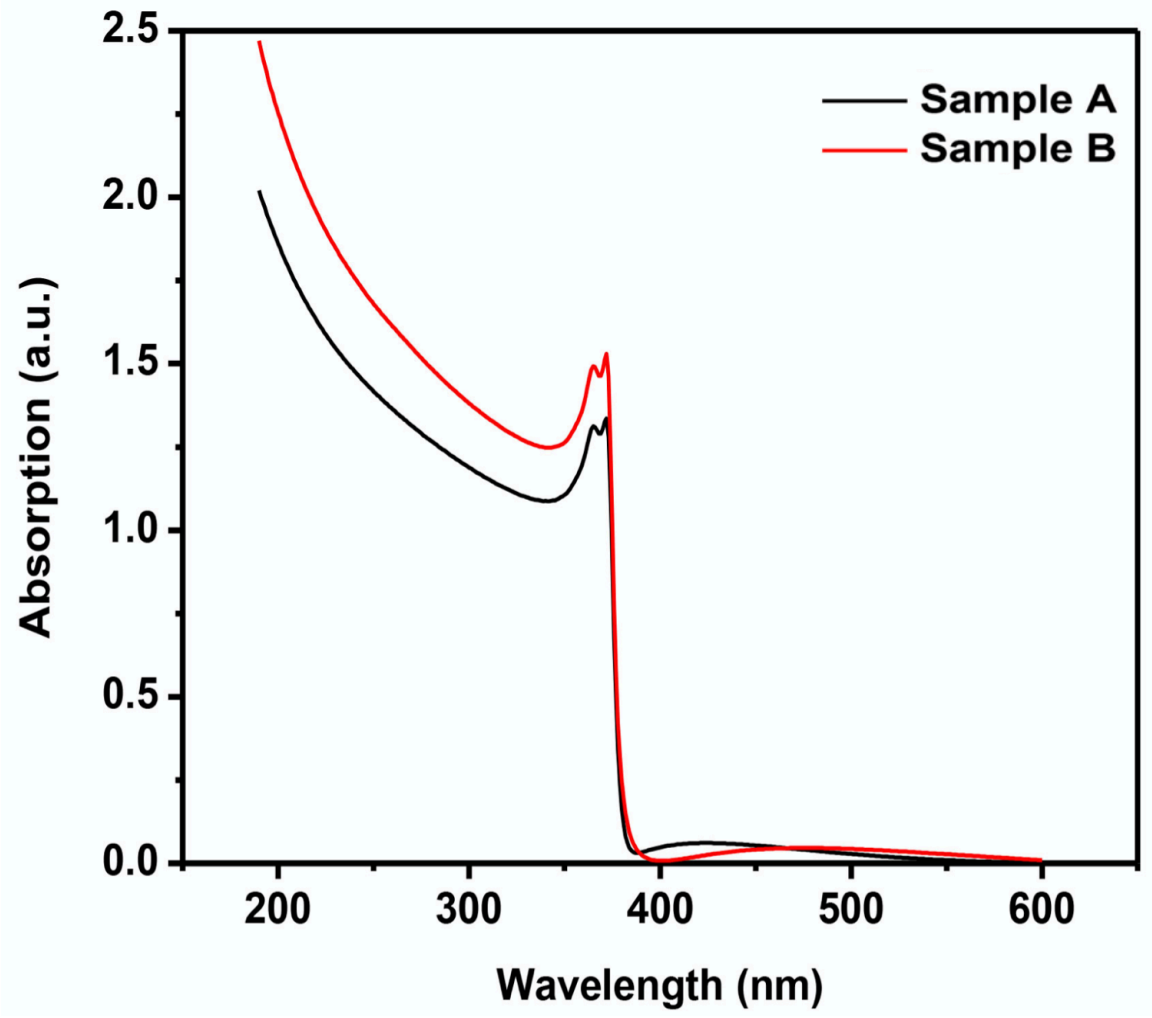

Figure. 3.1.3 Absorption spectrum of the ZnO samples annealed with (A) and without (B) oxygen ambient.

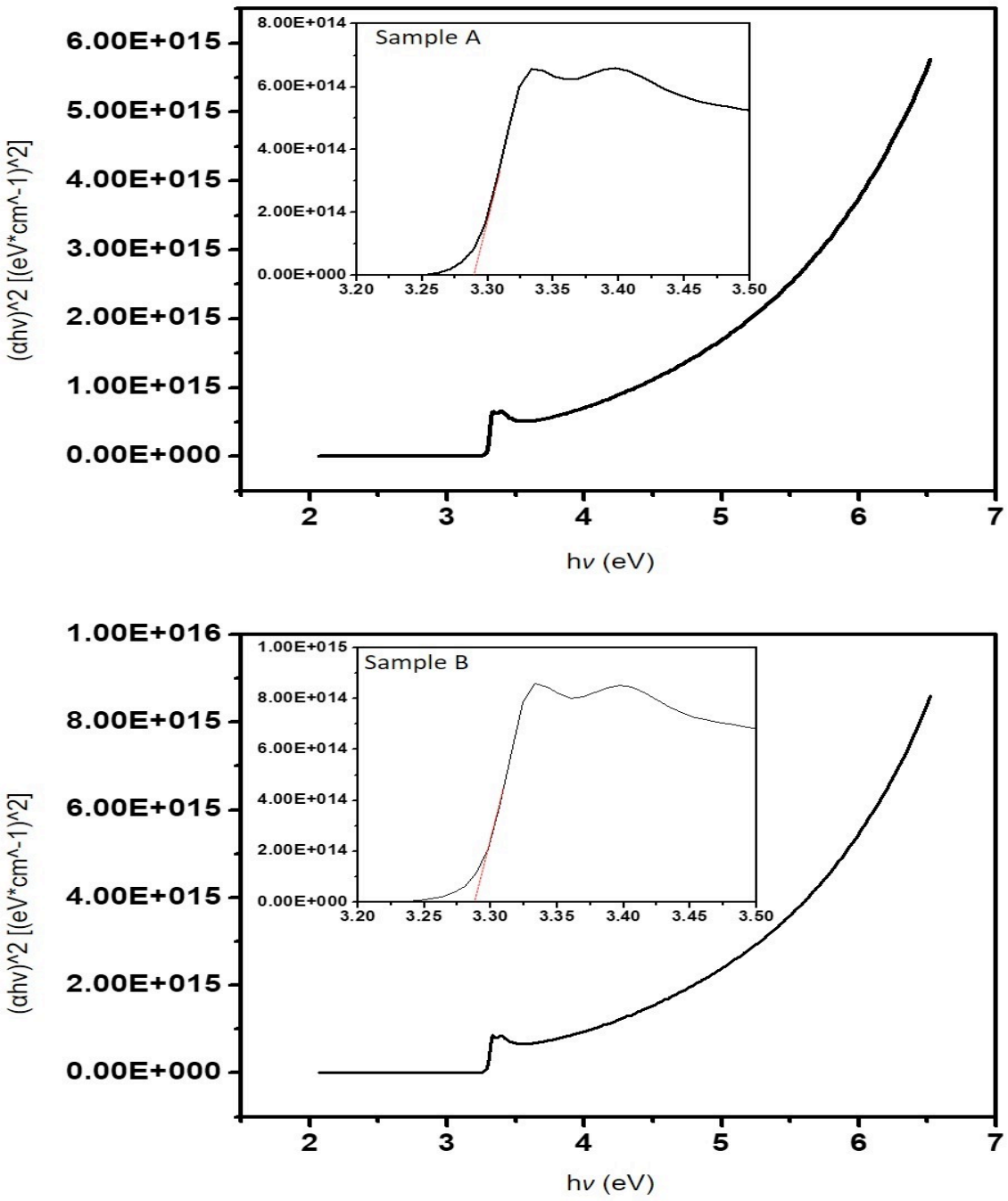

Figure. 3.1.4 Tauc plot of the ZnO samples annealed with (A) and without (B) oxygen ambient.

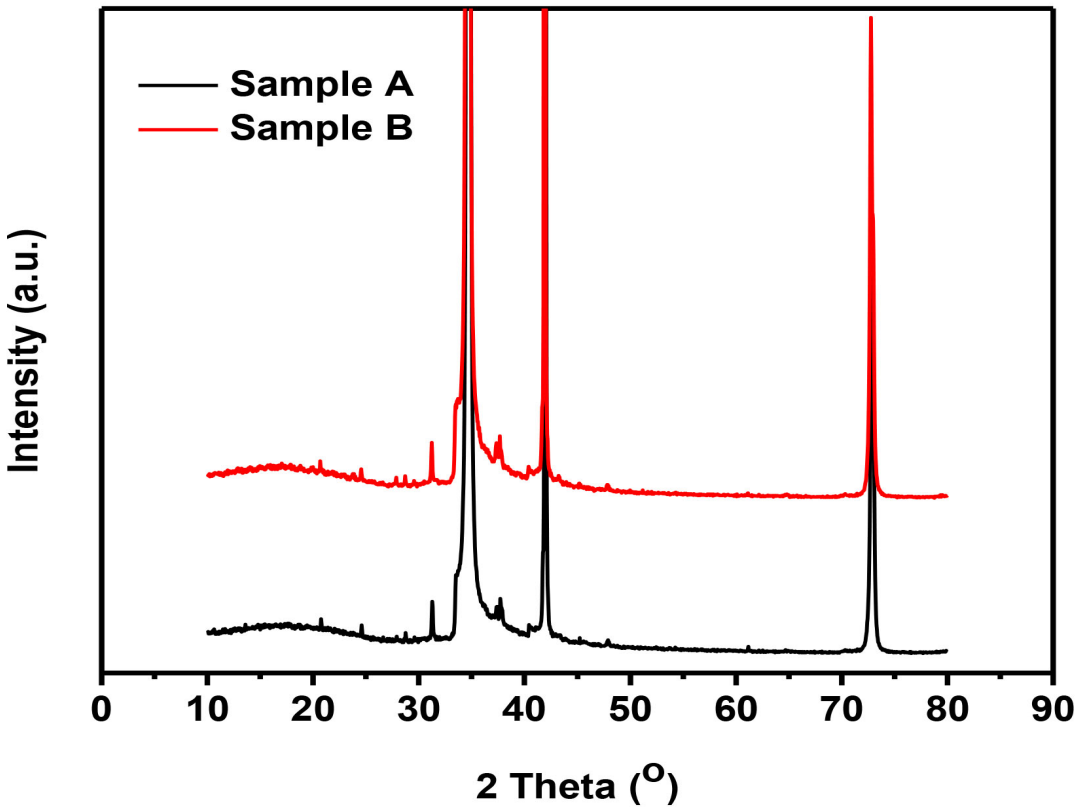

Figure. 3.1.5 XRD spectrum of the ZnO samples annealed with (A) and without (B) oxygen ambient.

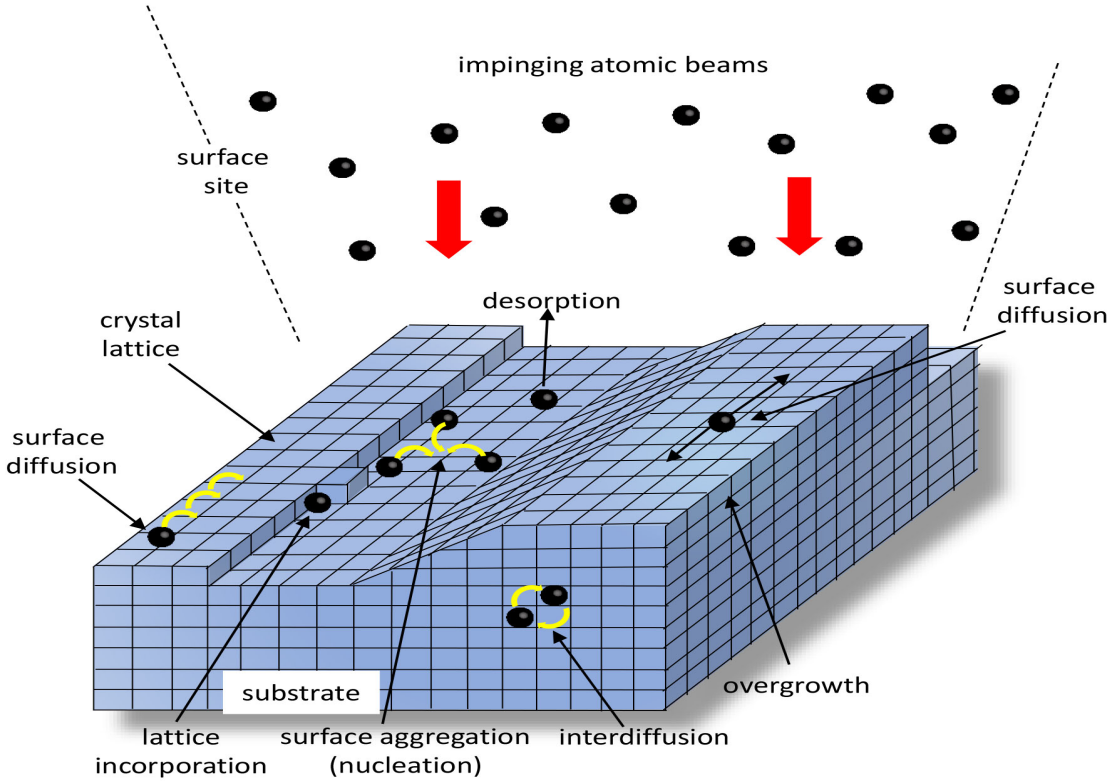

Figure. 3.2.1 A series of surface processes of thin film growth.

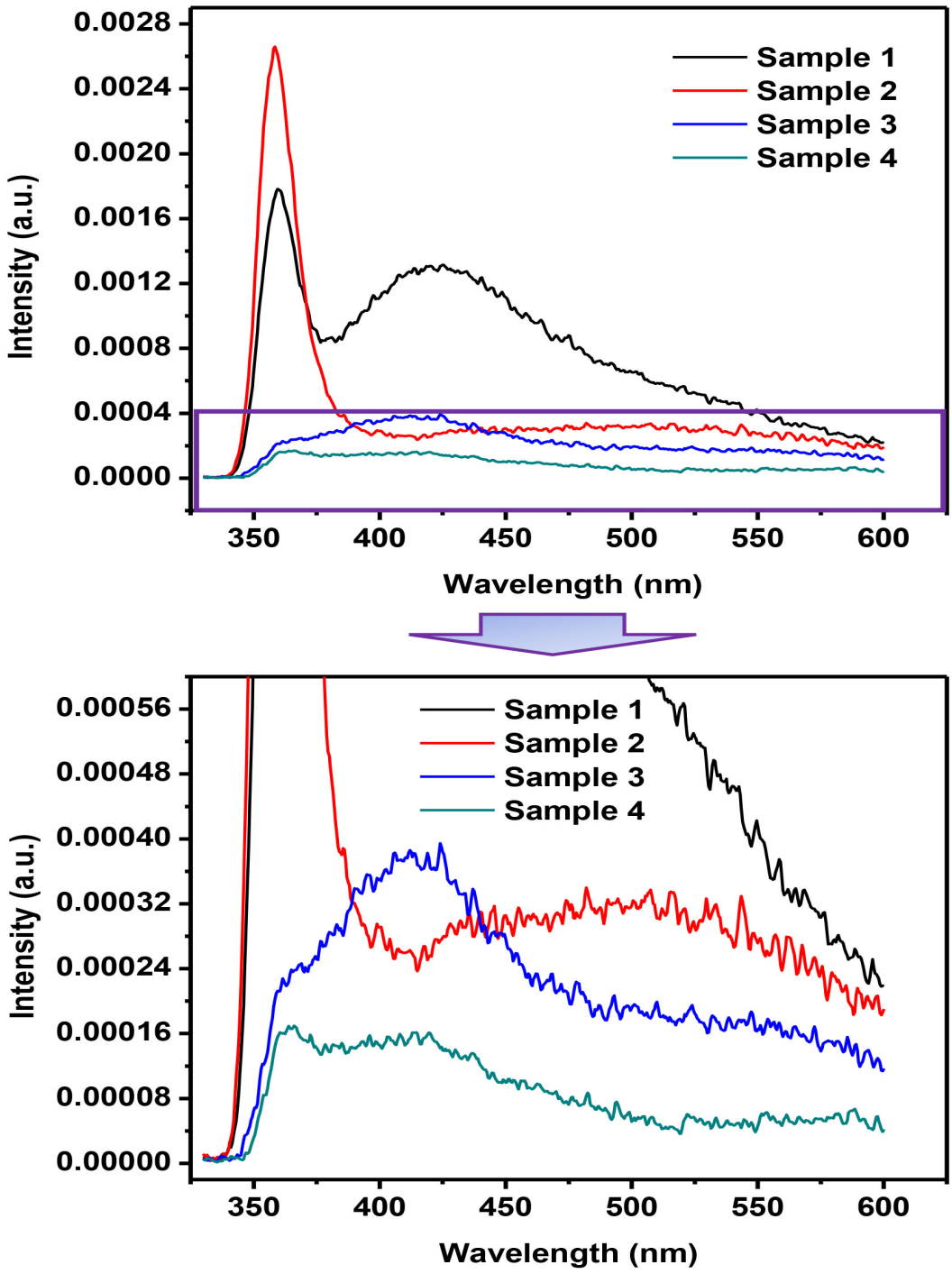

Figure. 3.2.2 The PL spectrum of 4 samples grown with different substrate temperature (sample 1 : 280 ˚C, sample 2 : 300 ˚C, sample 3 : 350 ˚C, sample 4 : 450 ˚C).

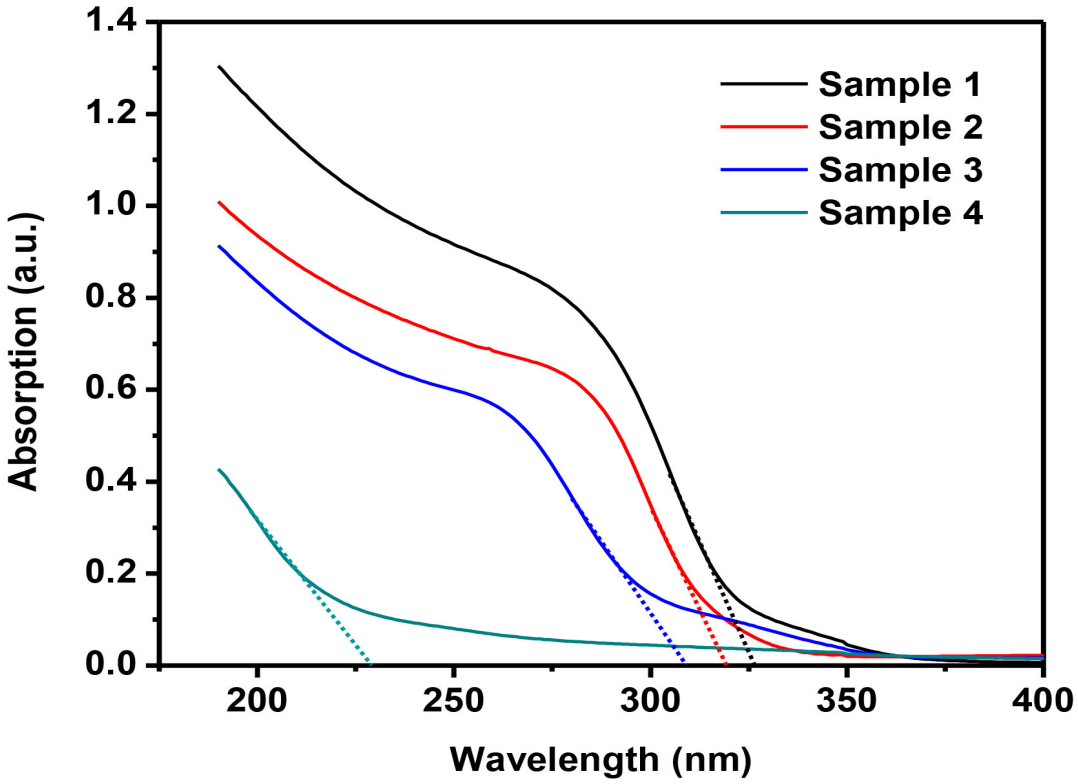

Figure. 3.2.3 The absorption spectrum of 4 samples grown with different substrate temperature (sample 1 : 280 ˚C, sample 2 : 300 ˚C, sample 3 : 350 ˚C, sample 4 : 450 ˚C).

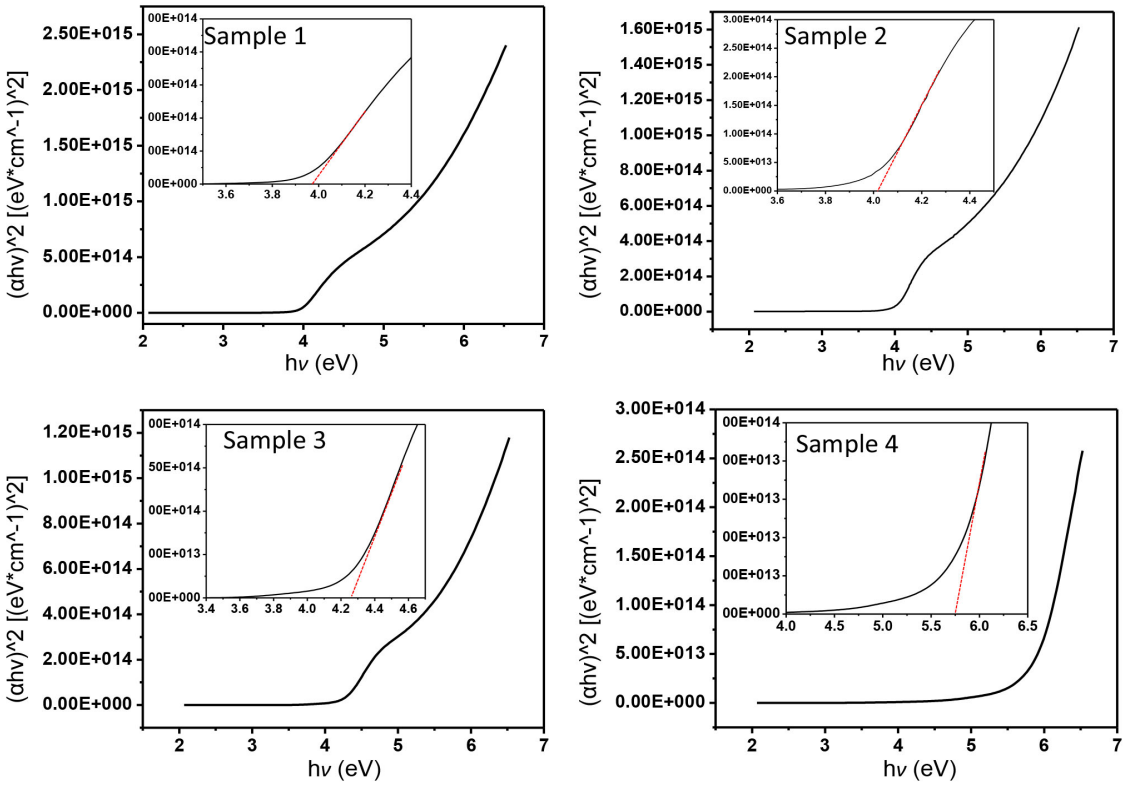

Figure. 3.2.4 The Tauc plot of 4 samples grown with different substrate temperature (sample 1 : 280 ˚C, sample 2 : 300 ˚C, sample 3 : 350 ˚C, sample 4 : 450 ˚C).

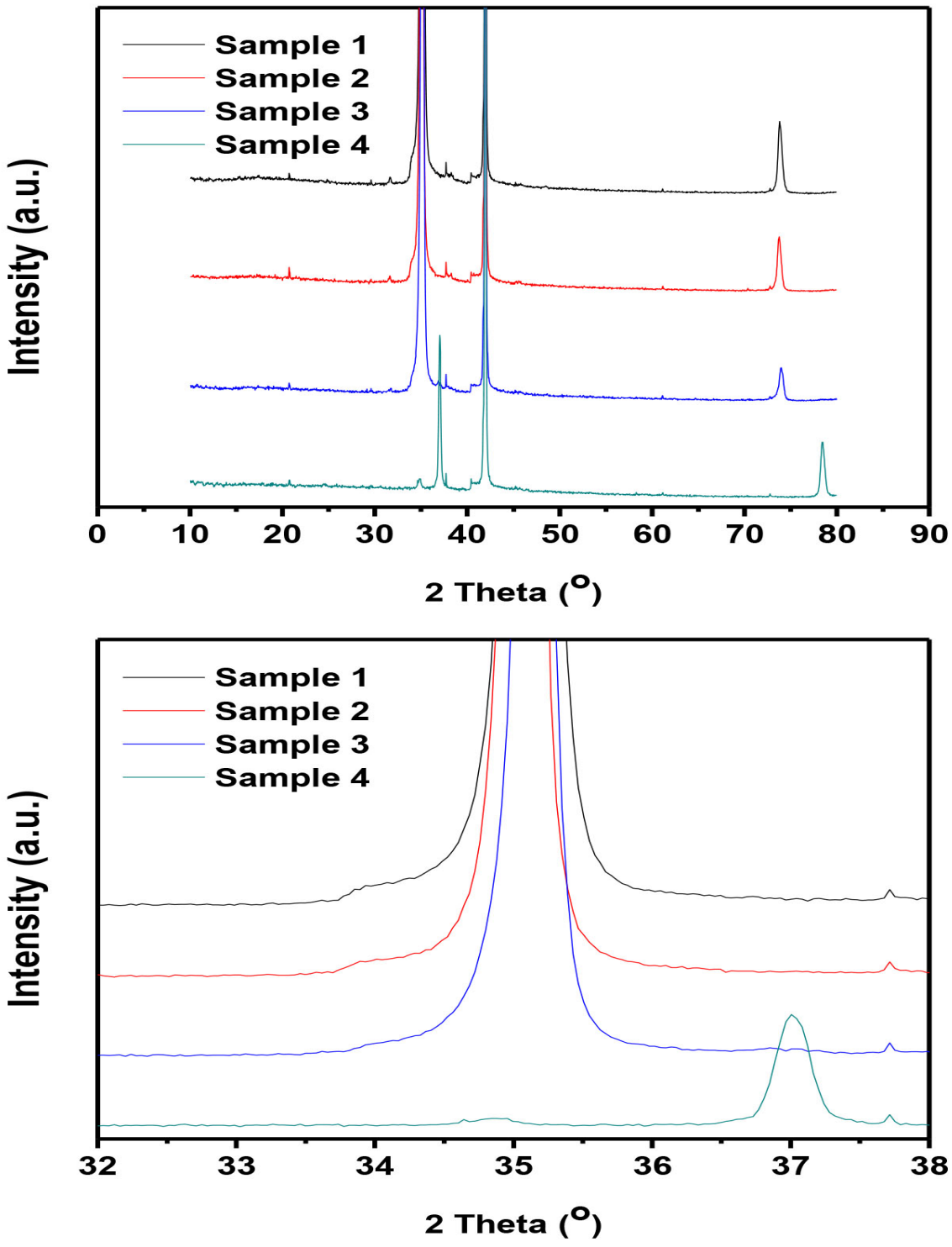

Figure. 3.2.5 XRD spectrum of 4 samples grown with different substrate temperature (sample 1 : 280 ˚C, sample 2 : 300 ˚C, sample 3 : 350 ˚C, sample 4 : 450 ˚C).

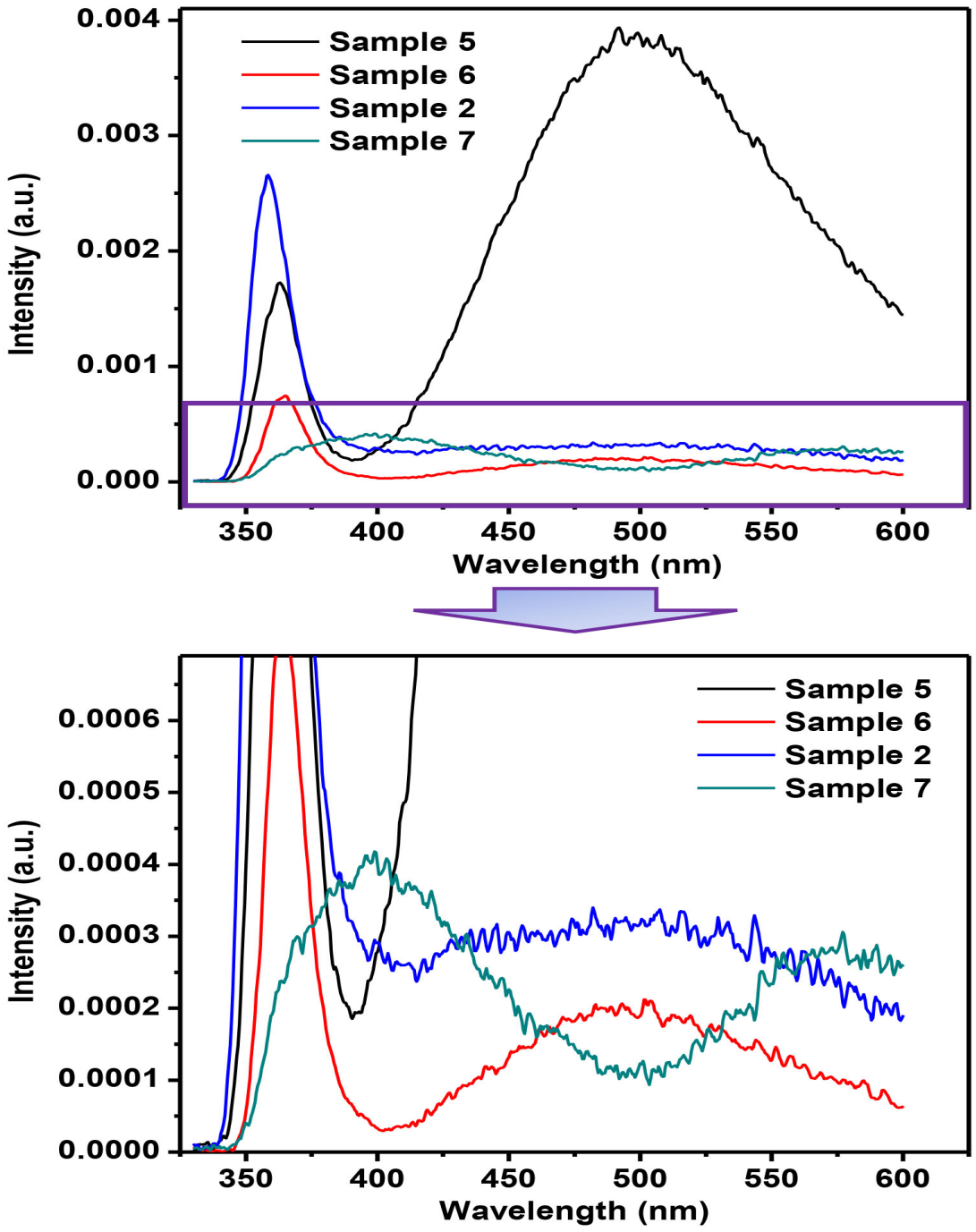

Figure. 3.2.6 PL spectrum of 4 samples grown with different Zn cell temperature (sample 5 : 305 ˚C, sample 6 : 295 ˚C, sample 2 : 285 ˚C, sample 7 : 275 ˚C).

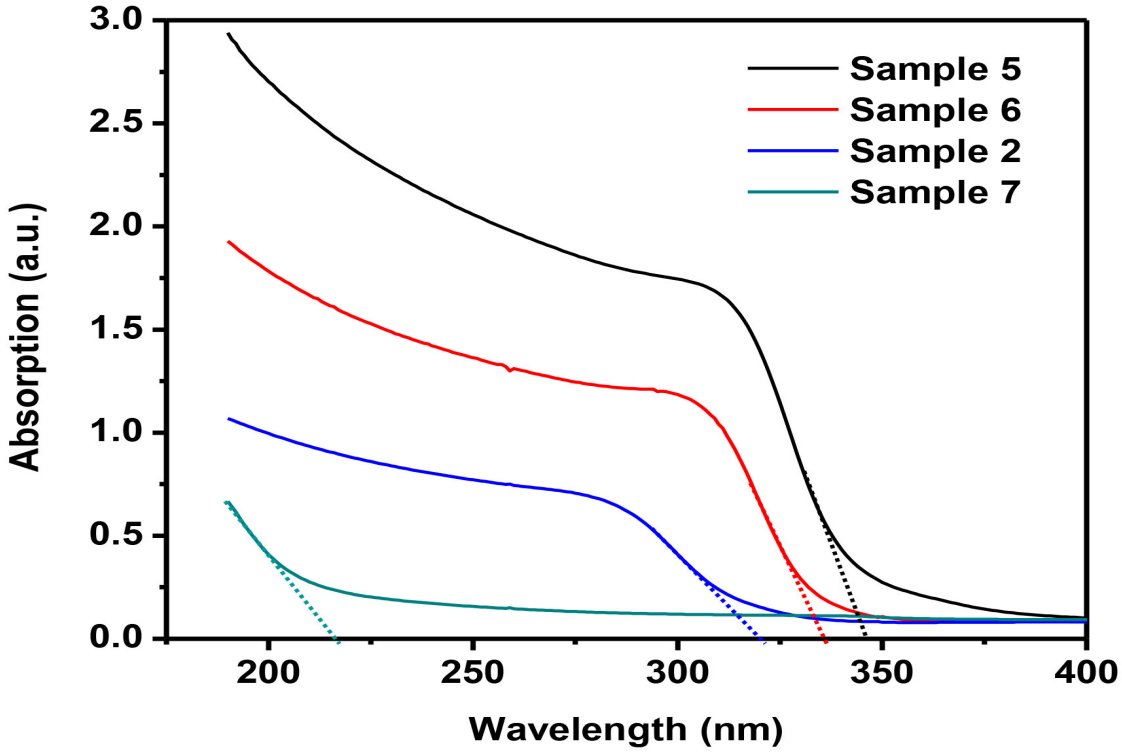

Figure. 3.2.7 Absorption spectrum of 4 samples grown with different Zn cell temperature (sample 5 : 305 ˚C, sample 6 : 295 ˚C, sample 2 : 285 ˚C, sample 7 : 275 ˚C).

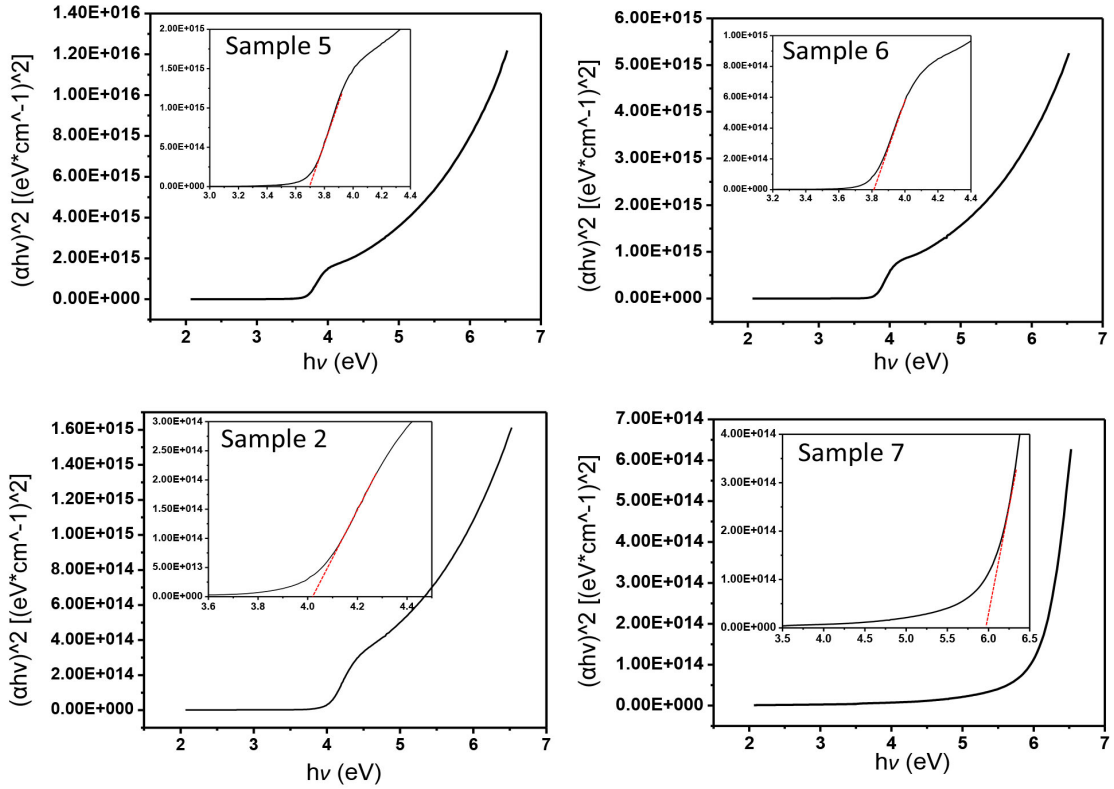

Figure. 3.2.8 Tauc plot of 4 samples grown with different Zn cell temperature (sample 5 : 305 ˚C, sample 6 : 295 ˚C, sample 2 : 285 ˚C, sample 7 : 275 ˚C).

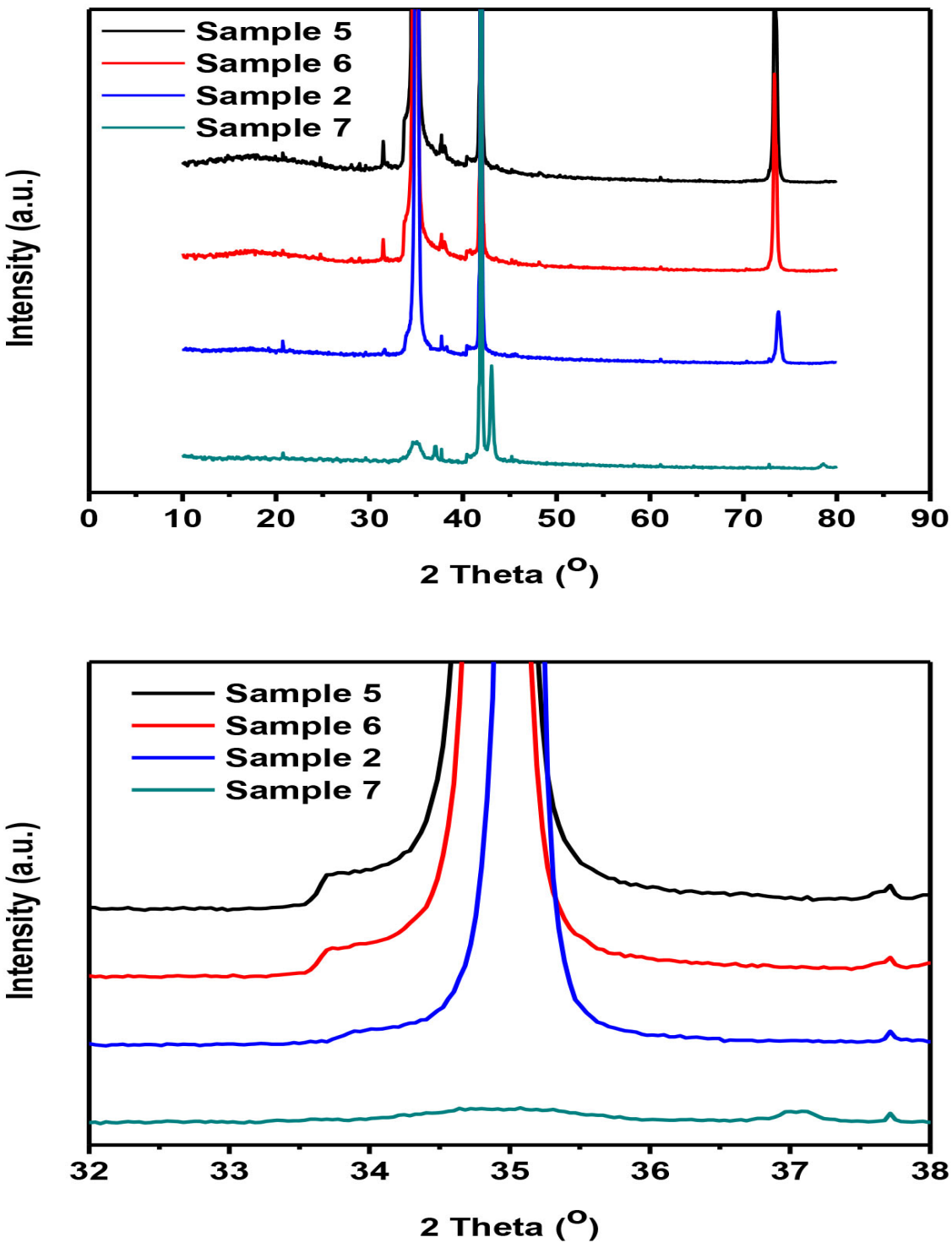

Figure. 3.2.9 XRD spectrum of 4 samples grown with different Zn cell temperature (sample 5 : 305 ˚C, sample 6 : 295 ˚C, sample 2 : 285 ˚C, sample 7 : 275 ˚C).

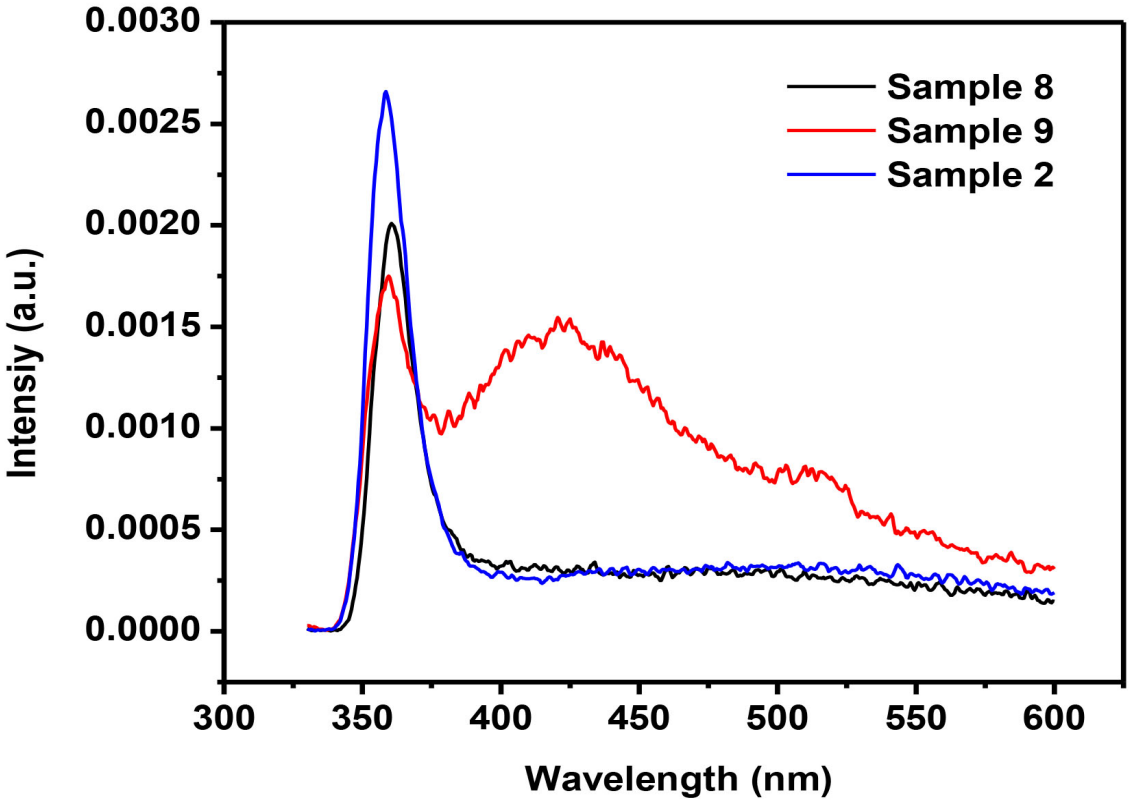

Figure. 3.2.10 PL spectrum of 3 samples grown with different buffer layer (sample 8 : MgO single layer buffer, sample 9 : ZnO single layer buffer, sample 2 : MgO/ZnO bi-layer buffer).

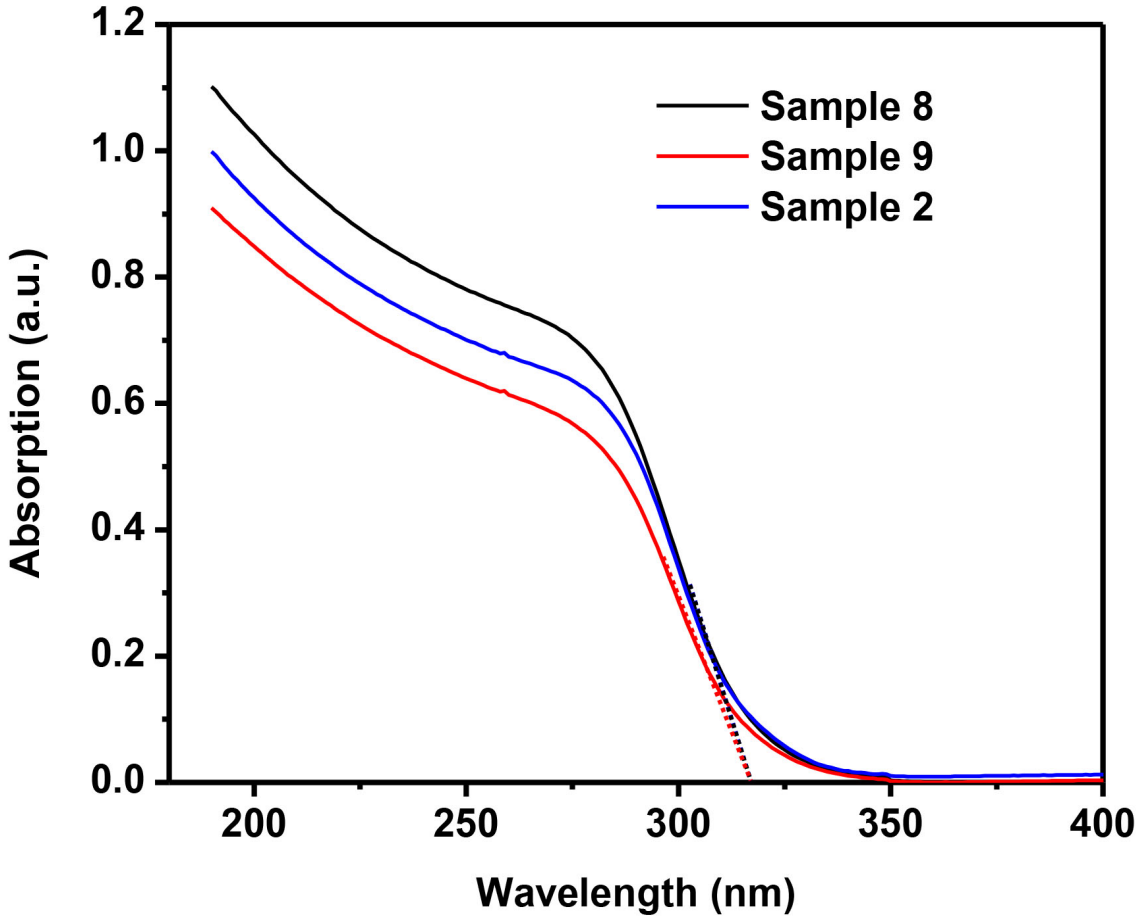

Figure. 3.2.11 Absorption spectrum of 3 samples grown with different buffer layer (sample 8 : MgO single layer buffer, sample 9 : ZnO single layer buffer, sample 2 : MgO/ ZnO bi-layer buffer).

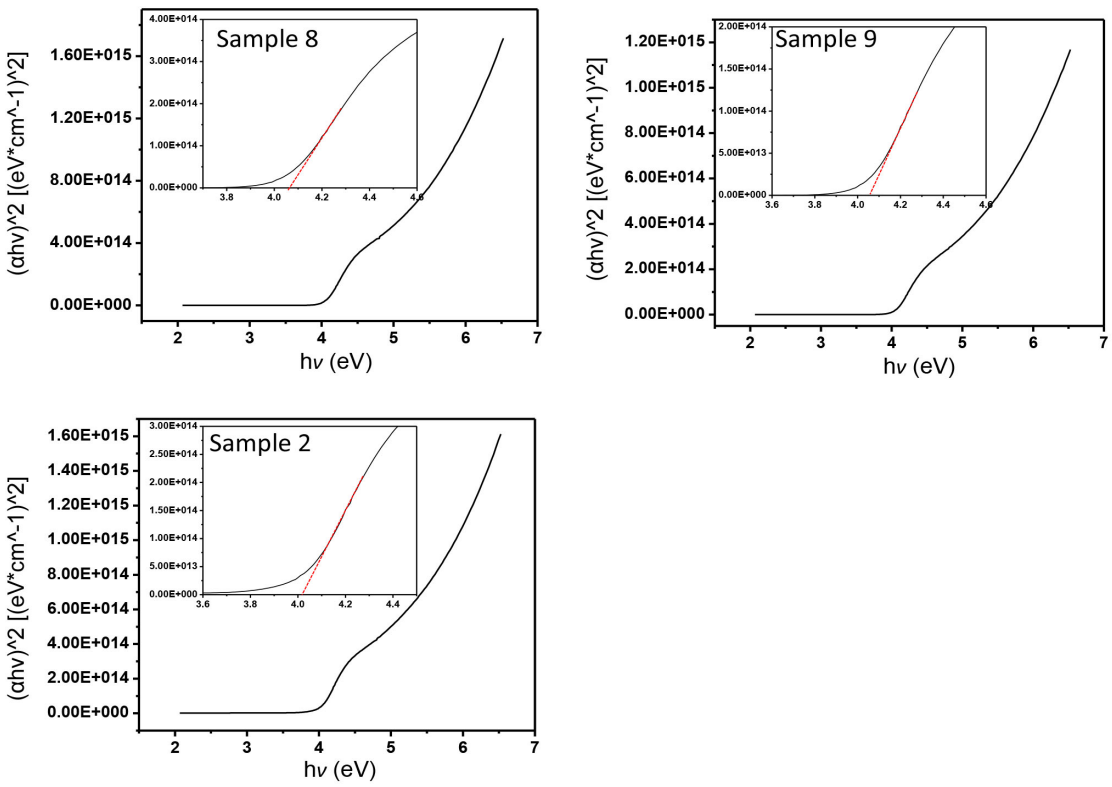

Figure. 3.2.12 Tauc plot of 3 samples grown with different buffer layer (sample 8 : MgO single layer buffer, sample 9 : ZnO single layer buffer, sample 2 : MgO/ZnO bi-layer buffer).

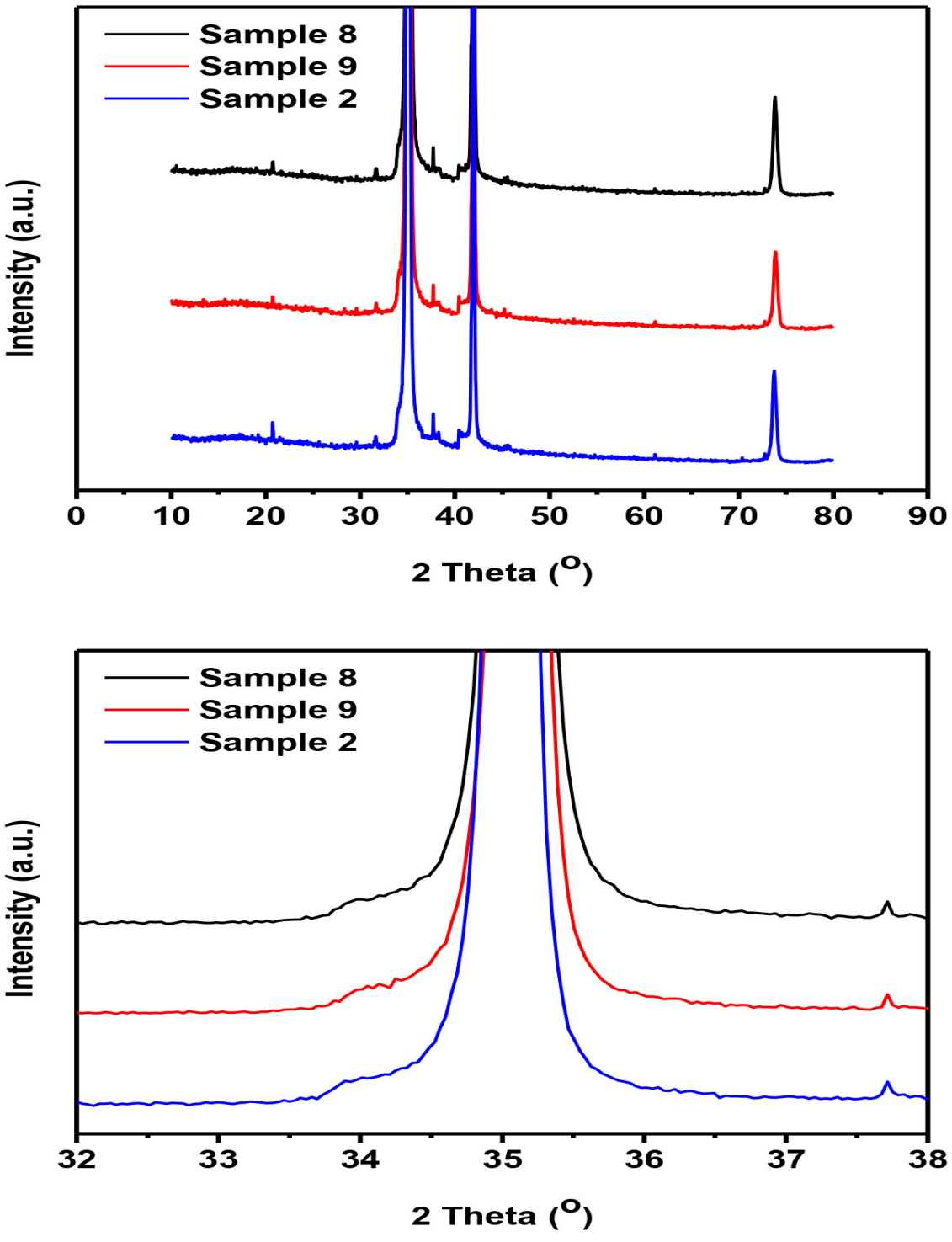

Figure. 3.2.13 XRD spectrum of 3 samples grown with different buffer layer (sample 8 : MgO single layer buffer, sample 9 : ZnO single layer buffer, sample 2 : MgO/ZnO bi-layer buffer).

Table

Sample #	Buffer layer	Substrate temperature	Cell temperature	Oxygen flow	Time
A	450 ˚C, O_2 1.5sccm MgO1.5'(450 ˚C)/ ZnO3.5' (305 ˚C)	300 ˚C	Zn 305 ˚C	2.5 sccm	2 hour
B	450 ˚C, O_2 1.5sccm MgO1.5'(450 ˚C)/ ZnO3.5' (305 ˚C)	300 ˚C	Zn 305 ˚C	2.5 sccm	2 hour

Table. 3.1 Growth conditions of 2 ZnO samples annealed with (A) and without (B) oxygen ambient.

Sample #	PL peak (nm)	Absorption edge	Band gap (eV)	XRD peak (2θ)
A	380 nm	379 nm	3.29 eV	34.641˚ (002)
B	378 nm	379 nm	3.29 eV	34.681˚ (002)

Table. 3.2 Characterization results of 2 ZnO samples annealed with (A) and without (B) oxygen ambient.

Sample #	Buffer layer	Substrate temperature	Cell temperature	Oxygen flow	Time
1	450 ˚C, O_2 1.5sccm MgO1.5'(450 ˚C)/ ZnO3.5' (305 ˚C)	280 ˚C	Zn 285 ˚C Mg 450 ˚C	2.5 sccm	2 hour
2	450 ˚C, O_2 1.5sccm MgO1.5'(450 ˚C)/ ZnO3.5' (305 ˚C)	300 ˚C	Zn 285 ˚C Mg 450 ˚C	2.5 sccm	2 hour
3	450 ˚C, O_2 1.5sccm MgO1.5'(450 ˚C)/ ZnO3.5' (305 ˚C)	350 ˚C	Zn 285 ˚C Mg 450 ˚C	2.5 sccm	2 hour
4	450 ˚C, O_2 1.5sccm MgO1.5'(450 ˚C)/ ZnO3.5' (305 ˚C)	450 ˚C	Zn 285 ˚C Mg 450 ˚C	2.5 sccm	2 hour

Table. 3.3 Growth conditions of 4 MgZnO samples grown with different substrate temperature.

Sample #	PL peak (nm)	Absorption edge	Band gap (eV)	XRD peak (2θ)
1	360 nm	322 nm	3.95 eV	35.075˚ (002)
2	358 nm	318 nm	4.04 eV	35.075˚ (002)
3	N/A	305 nm	4.22 eV	35.155˚ (002)
4	N/A	222 nm	5.83 eV	37.005˚ (111)

Table. 3.4 Characterization results of 4 MgZnO samples grown with different substrate temperature.

Sample #	Buffer layer	Substrate temperature	Cell temperature	Oxygen flow	Time
5	450 ˚C, O_2 1.5sccm MgO1.5'(450 ˚C)/ ZnO3.5' (305 ˚C)	300 ˚C	Zn 305 ˚C Mg 450 ˚C	2.5 sccm	2 hour
6	450 ˚C, O_2 1.5sccm MgO1.5'(450 ˚C)/ ZnO3.5' (305 ˚C)	300 ˚C	Zn 295 ˚C Mg 450 ˚C	2.5 sccm	2 hour
2	450 ˚C, O_2 1.5sccm MgO1.5'(450 ˚C)/ ZnO3.5' (305 ˚C)	300 ˚C	Zn 285 ˚C Mg 450 ˚C	2.5 sccm	2 hour
7	450 ˚C, O_2 1.5sccm MgO1.5'(450 ˚C)/ ZnO3.5' (305 ˚C)	300 ˚C	Zn 275 ˚C Mg 450 ˚C	2.5 sccm	2 hour

Table. 3.5 Growth conditions of 4 MgZnO samples grown with different Zn cell temperature.

Sample #	PL peak (nm)	Absorption edge	Band gap (eV)	XRD peak (2θ)
5	363 nm	342 nm	3.71 eV	34.877˚ (002)
6	365 nm	337 nm	3.81 eV	34.877˚ (002)
2	358 nm	318 nm	4.04 eV	35.075˚ (002)
7	N/A	219 nm	6.13 eV	35.08˚ (002) 42.007˚ (200)

Table. 3.6 Characterization results of 4 MgZnO samples grown with different Zn cell temperature.

Sample #	Buffer layer	Substrate temperature	Cell temperature	Oxygen flow	Time
8	450 ˚C, O_2 1.5sccm MgO1.5'(450 ˚C)	300 ˚C	Zn 285 ˚C Mg 450 ˚C	2.5 sccm	2 hour
9	450 ˚C, O_2 1.5sccm ZnO3.5' (305 ˚C)	300 ˚C	Zn 285 ˚C Mg 450 ˚C	2.5 sccm	2 hour
2	450 ˚C, O_2 1.5sccm MgO1.5'(450 ˚C)/ ZnO3.5' (305 ˚C)	300 ˚C	Zn 285 ˚C Mg 450 ˚C	2.5 sccm	2 hour

Table. 3.7 Growth conditions of 3 MgZnO samples grown with different buffer layer.

Sample #	PL peak (nm)	Absorption edge	Band gap (eV)	XRD peak (2θ)
8	361 nm	317 nm	4.05 eV	35.115˚ (002)
9	360 nm	316 nm	4.05 eV	35.115˚ (002)
2	358 nm	318 nm	4.04 eV	35.075˚ (002)

Table. 3.8 Characterization results of 3 MgZnO samples grown with different buffer layer.

Chapter 4

Summary

In conclusion, we have demonstrated the ZnO thin films and its ternary alloy MgZnO thin films grown by plasma-assisted MBE. In this thesis we have successfully fabricated the MgZnO ternary thin films of band gap energy up to 4.22 eV without phase separation. This result has reached the highest Mg concentration of 37.3% for single wurtzite MgZnO thin film which has been published in recent studies (Figure 1.3). The characterizations of ZnO and MgZnO thin films have been investigated which are photoluminescence (PL), UV-visible absorption and X-ray diffraction (XRD). We have analyzed the characterizations of MgZnO thin films based different growth conditions which are growth temperature, effusion cell temperature and buffer layer. For the characterizations of growth temperature series, the results indicate that the Mg incorporation increases as the substrate temperature increases. Furthermore, the thickness of the thin films decreases as the substrate temperature increases due to the larger desorption rate than the adsorption rate. In terms of the effusion cell series, the characterizations show that the Mg incorporation increases as the Zn cell temperature decreases. This result is expectable since lower impinging speed of Zn atoms allows higher Mg incorporation into ZnO. For the buffer layer series, the characterization results show that different buffer layers barely affect on the Mg incorporation. However, it affects the native defects of the thin films due to the switching of the polarity. Most of the ZnO thin films have unintentional O-polar of polarity. Inserting a MgO buffer layer

between substrate and active layer which exceed the critical thickness (~2 nm) can change the polarity from O-polar to Zn-polar. The change of the polarity leads to the defect peak elimination of PL spectrum because O-polar ZnO thin films generate more point defects than Zn-polar. In this thesis we mainly focus on the optical and structural properties of single wurtzite MgZnO ternary alloy, the electrical property still requires further examinations.

Reference

[1] Y.F. Chen, D.M. Bagnall, H.J. Koh, K.T. Park, K. Hiraga, Z.Q. Zhu, T. Yao, Plasma assisted molecular beam epitaxy of ZnO on c-plane sapphire: Growth and characterization, J Appl Phys 84(7) (1998) 3912-3918.

[2] P. Capper, S. Kasap, A. Willoughby, Zinc oxide materials for electronic and optoelectronic device applications, John Wiley & Sons2011.

[3] D.C. Reynolds, D.C. Look, B. Jogai, Optically pumped ultraviolet lasing from ZnO, Solid State Communications 99(12) (1996) 873-875.

[4] S.E. Harrison, Conductivity and Hall effect of ZnO at low temperatures, Physical Review 93(1) (1954) 52.

[5] A. Janotti, C.G. Van de Walle, Oxygen vacancies in ZnO, Applied Physics Letters 87(12) (2005) 122102.

[6] L. Vlasenko, G. Watkins, Optical detection of electron paramagnetic resonance for intrinsic defects produced in ZnO by 2.5-MeV electron irradiation in situ at 4.2 K, Physical Review B 72(3) (2005) 035203.

[7] L. Liu, Z. Mei, A. Tang, A. Azarov, A. Kuznetsov, Q.-K. Xue, X. Du, Oxygen vacancies: The origin of n-type conductivity in ZnO, Physical Review B 93(23) (2016) 235305.

[8] A. Janotti, C.G. Van de Walle, Fundamentals of zinc oxide as a semiconductor, Reports on progress in physics 72(12) (2009) 126501.

[9] X. Chen, J. Kang, The structural properties of wurtzite and rocksalt MgxZn1− xO, Semiconductor Science and Technology 23(2) (2008) 025008.

[10] Y. Hu, B. Cai, Z. Hu, Y. Liu, S. Zhang, H. Zeng, The impact of Mg content on the structural, electrical and optical properties of MgZnO alloys: a first principles study, Current Applied Physics 15(3) (2015) 423-428.

[11] A. Ohtomo, M. Kawasaki, T. Koida, K. Masubuchi, H. Koinuma, Y. Sakurai, Y. Yoshida, T. Yasuda, Y. Segawa, Mg x Zn 1− x O as a II–VI widegap semiconductor alloy, Applied Physics Letters 72(19) (1998) 2466-2468.

[12] W. Yang, S. Hullavarad, B. Nagaraj, I. Takeuchi, R. Sharma, T. Venkatesan, R. Vispute, H. Shen, Compositionally-tuned epitaxial cubic Mg x Zn 1− x O on Si (100) for deep ultraviolet photodetectors, Applied Physics Letters 82(20) (2003) 3424-3426.

[13] H. Yin, J. Chen, Y. Wang, J. Wang, H. Guo, Composition dependent band offsets of ZnO and its ternary alloys, Scientific reports 7 (2017) 41567.

[14] A.Y. Cho, J. Arthur, Molecular beam epitaxy, Progress in solid state chemistry 10 (1975) 157-191.

[15] M.A. Herman, H. Sitter, Molecular beam epitaxy: fundamentals and current status, Springer Science & Business Media2012.

[16] M. Johnson, S. Fujita, W. Rowland, W. Hughes, J. Cook, J. Schetzina, MBE growth and properties of ZnO on sapphire and SiC substrates, Journal of Electronic Materials 25(5) (1996) 855-862.

[17] K. Sakurai, M. Kanehiro, K. Nakahara, T. Tanabe, S. Fujita, S. Fujita, Effects of oxygen plasma condition on MBE growth of ZnO, Journal of crystal growth 209(2-3) (2000) 522-525.

[18] F. Vigue, P. Vennegues, S. Vezian, M. Laügt, J.-P. Faurie, Defect characterization in ZnO layers grown by plasma-enhanced molecular-beam epitaxy on (0001) sapphire substrates, Applied Physics Letters 79(2) (2001) 194-196.

[19] H. Kato, M. Sano, K. Miyamoto, T. Yao, Effect of O/Zn flux ratio on crystalline quality of ZnO films grown by plasma-assisted molecular beam epitaxy, Japanese Journal of Applied Physics 42(4S) (2003) 2241.

[20] N. Kawamoto, M. Fujita, T. Tatsumi, Y. Horikoshi, Growth of ZnO on Si substrate by plasma-assisted molecular beam epitaxy, Japanese journal of applied physics 42(12R) (2003) 7209.

[21] M. Cho, A. Setiawan, H. Ko, S. Hong, T. Yao, ZnO epitaxial layers grown on c-sapphire substrate with MgO buffer by plasma-assisted molecular beam epitaxy (P-MBE), Semiconductor science and technology 20(4) (2005) S13.

[22] A. El-Shaer, A.C. Mofor, A. Bakin, M. Kreye, A. Waag, High-quality ZnO layers grown by MBE on sapphire, Superlattices and Microstructures 38(4-6) (2005) 265-271.

[23] C. Pan, C. Tu, J. Song, G. Cantwell, C. Lee, B. Pong, G. Chi, Photoluminescence of ZnO films grown by plasma-assisted molecular beam epitaxy, Journal of crystal growth 282(1-2) (2005) 112-116.

[24] M.S. Kim, T.H. Kim, D.Y. Kim, G.S. Kim, H.Y. Choi, M.Y. Cho, S.M. Jeon, J.S. Kim, J.S. Kim, D. Lee, Improvement in crystallinity and optical properties of ZnO epitaxial layers by thermal annealed ZnO buffer layers with oxygen plasma, Journal of Crystal Growth 311(14) (2009) 3568-3572.

[25] Y. Chen, H.-J. Ko, S.-K. Hong, T. Yao, Layer-by-layer growth of ZnO epilayer on Al 2 O 3 (0001) by using a MgO buffer layer, Applied Physics Letters 76(5) (2000) 559-561.

[26] T. Takagi, H. Tanaka, S. Fujita, S. Fujita, Molecular Beam Epitaxy of High Magnesium Content Single-Phase Wurzite MgxZn1-xO Alloys (x≃ 0.5) and Their Application to Solar-Blind Region Photodetectors, Japanese journal of applied physics 42(4B) (2003) L401.

[27] Y. Nishimoto, K. Nakahara, D. Takamizu, A. Sasaki, K. Tamura, S. Akasaka, H. Yuji, T. Fujii, T. Tanabe, H. Takasu, Plasma-assisted molecular beam epitaxy of high optical quality MgZnO films on Zn-polar ZnO substrates, Applied physics express 1(9) (2008) 091202.

[28] H. Huang, F. Liu, J. Sun, J. Zhao, Z. Hu, Z. Li, X. Zhang, Y. Wang, Effect of MgO buffer layer thickness on the electrical properties of MgZnO thin film transistors fabricated by plasma assisted molecular beam epitaxy, Applied Surface Science 257(24) (2011) 10721-10724.

[29] A. Redondo-Cubero, A. Hierro, J.-M. Chauveau, K. Lorenz, G. Tabares, N. Franco, E. Alves, E. Muñoz, Single phase a-plane MgZnO epilayers for UV optoelectronics: substitutional behaviour of Mg at large contents, CrystEngComm 14(5) (2012) 1637-1640.

[30] W.V. Schoenfeld, M. Wei, R.C. Boutwell, H. Liu, High response solar-blind MgZnO photodetectors grown by molecular beam epitaxy, Oxide-based Materials and Devices V, International Society for Optics and Photonics, 2014, p. 89871P.

[31] M. Suja, S.B. Bashar, B. Debnath, L. Su, W. Shi, R. Lake, J. Liu, Electrically driven deep ultraviolet MgZnO lasers at room temperature, Scientific reports 7(1) (2017) 2677.

[32] K. Mahmood, B. Samaa, Influence of Annealing Treatment on Structural, Optical,

Electric, and Thermoelectric Properties of MBE-Grown ZnO, Journal of Experimental and Theoretical Physics 126(6) (2018) 766-771.

[33] L. Wang, N. Giles, Temperature dependence of the free-exciton transition energy in zinc oxide by photoluminescence excitation spectroscopy, J Appl Phys 94(2) (2003) 973-978.

[34] D. Reynolds, D.C. Look, B. Jogai, Fine structure on the green band in ZnO, J Appl Phys 89(11) (2001) 6189-6191.

[35] H. Chen, S. Gu, K. Tang, S. Zhu, Z. Zhu, J. Ye, R. Zhang, Y. Zheng, Origins of green band emission in high-temperature annealed N-doped ZnO, Journal of Luminescence 131(6) (2011) 1189-1192.

[36] F. Fabbri, M. Villani, A. Catellani, A. Calzolari, G. Cicero, D. Calestani, G. Calestani, A. Zappettini, B. Dierre, T. Sekiguchi, Zn vacancy induced green luminescence on non-polar surfaces in ZnO nanostructures, Scientific reports 4 (2014) 5158.

[37] C. Tan, D. Sun, X. Tian, Y. Huang, First-principles investigation of phase stability, electronic structure and optical properties of MgZnO monolayer, Materials 9(11) (2016) 877.

[38] K. Nagai, A simple rate equation useful for adsorption systems: Analyses of thermal desorption spectra, Surface science 176(1-2) (1986) 193-218.

[39] S.L. Schroeder, M. Gottfried, Temperature-programmed desorption (TPD) thermal desorption spectroscopy (TDS), Adv. Phys. Chem. Lab, FU Berlin, June 2002 (2002).

[40] D. Wood, J. Tauc, Weak absorption tails in amorphous semiconductors, Physical Review B 5(8) (1972) 3144.

[41] I. Takeuchi, W. Yang, K.-S. Chang, M. Aronova, T. Venkatesan, R. Vispute, L. Bendersky, Monolithic multichannel ultraviolet detector arrays and continuous phase evolution in Mg x Zn 1− x O composition spreads, J Appl Phys 94(11) (2003) 7336-7340.

[42] H. Kato, K. Miyamoto, M. Sano, T. Yao, Polarity control of ZnO on sapphire by varying the MgO buffer layer thickness, Applied Physics Letters 84(22) (2004) 4562-4564.

[43] Y.-M. Yu, B.-G. Liu, Contrasting morphologies of O-rich ZnO epitaxy on Zn-and O-

polar thin film surfaces: Phase-field model, Physical Review B 77(19) (2008) 195327.